Geochimica et Cosmochimica Acta 341 (2023) 183–199

Contents lists available at ScienceDirect

Geochimica et Cosmochimica Acta

journal homepage: www.elsevier.com/locate/gca

Early diagenetic processes in an iron-dominated marine depositional system

Maria C. Figueroa [a,*], Sebastiaan J. van de Velde [a,b,c], Daniel D. Gregory [a,d], Sydnie Lemieux [e], Jeana Drake [f], Tina Treude [e,f], Nathaniel Kemnitz [g], William Berelson [g], Konstantin Choumiline [a], Steven Bates [a], Ravi Kukkadapu [h], Marilyn Fogel [a,1], Natascha Riedinger [i], Timothy W. Lyons [a]

[a] Department of Earth and Planetary Sciences, University of California, Riverside, CA 92521, USA
[b] Department of Geoscience, Environment and Society, Université Libre de Bruxelles, Brussels, Belgium
[c] Operational Directorate Natural Environment, Royal Belgian Institute of Natural Sciences, Brussels, Belgium
[d] Department of Earth Sciences, University of Toronto, Toronto, Ontario M5S 3B1, Canada
[e] Department of Atmospheric and Oceanic Sciences, University of California, Los Angeles, CA 90095, USA
[f] Department of Earth, Planetary, and Space Sciences, University of California, Los Angeles, CA 90095, USA
[g] Department of Earth Sciences, University of Southern California, Los Angeles, CA 90089, U.S.A
[h] Environmental Molecular Sciences Laboratory, Pacific Northwest National Laboratory, Richland, WA 99354, USA
[i] Boone Pickens School of Geology, Oklahoma State University, Stillwater, OK 74078, USA

ARTICLE INFO

Article history:
Received 6 February 2022
Accepted 23 November 2022
Available online 24 November 2022
Associate editor: Caroline Slomp

Keywords:
Early diagenesis
Reactive iron
Redox cycling
Marine sediments
Iron sulfides

ABSTRACT

The early diagenetic interplay between reactive iron, sulfur, and organic matter in the bathymetrically isolated Santa Monica Basin (SMB) sediments are investigated in this study. We explore solid-phase and porewater profiles from the basin, supplemented with a transect from 71 to 907 m water depth that includes oxygenated (>60 μM O_2) bottom waters near the coast and oxygen-deficient waters (~4 μM O_2) in the basin. The geochemical data of the basin sediments are further scrutinized by means of reactive transport modeling.

The results show that the basin sediments do not follow the traditional geochemical signatures of oxygen-deficient settings. A lack of dissolved sulfide accumulation and sulfurized iron persists despite the sediments being deposited under reducing conditions (without bioturbation/bioirrigation), strong organic carbon input (TOC up to 5.0 wt%), and active dissimilatory sulfate reduction. Not only did we find an exceptional enrichment in highly reactive Fe in the surface sediments (~45 % of total Fe), but the enrichment of reactive Fe, including ferrihydrite, persists downcore and coexists with high levels of dissolved Fe. The enhanced preservation of Fe oxides and lack of iron-sulfide precipitation is in part explained by detection via Mössbauer spectra of iron oxides bounded to organic matter (Fe[III]-OM coprecipitates).

The modeled Fe budget shows that most of the Fe oxides in the surface sediments are internally recycled by upward diffusion and subsequent oxidation of Fe^{2+}. Sulfide oxidation coupled to Fe reduction effectively precludes sulfide accumulation while enhancing build-up of dissolved Fe, fueling the Fe cycle within the first 5 cm depth. Continuous reoxidation of Fe^{2+} enhances the formation of Fe(III)-OM coprecipitates, limiting the amount of reactive organic matter. In the unavailability of labile organic matter, other than within the uppermost layers, the organic-rich sediment profiles are dominated by Fe cycling that limits the production and preservation of sulfides and enhances the preservation of Fe oxides and organic carbon. This study highlights key local controls on Fe availability in marginal basins and describes an intricate biogeochemical C-Fe-S cycling in modern and possibly ancient marine systems with important implications for Fe availability in the marine realm.

1. Introduction

The highly heterogenous nature of continental margins can impact our understanding of redox reactions and diagenetic

* Corresponding author.
E-mail address: mfigu012@ucr.edu (M.C. Figueroa).
[1] Deceased.

https://doi.org/10.1016/j.gca.2022.11.026
0016-7037/

processes, further complicating the validation of paleoredox proxies. Specifically, the iron cycle and its role in carbon and sulfur burial is a particularly intricate process that is often oversimplified. The availability of iron as a micronutrient is critical for primary production (Raiswell and Canfield, 2012, and references therein), but given its low solubility under oxidizing conditions it is usually low in the open ocean. Various continental margins, however, are proximal to iron sources (e.g., estuaries; Severmann et al., 2010) and can promote high primary production. Moreover, sediments can be an important source of iron to the overlying water column (Berelson et al., 2003; Elrod et al., 2004; Severmann et al., 2010). Upwelling events, in particular, can move iron from the benthic zone towards the water column (Lohan and Bruland, 2008).

During early diagenesis, iron (Fe) is metabolically cycled between reduced and oxidized chemical forms, and the resulting flow of electrons is tied to reactions with other redox-sensitive elements, including oxygen, carbon, nitrogen, and sulfur. The availability of reactive Fe, meaning the Fe that may react with sulfide during early diagenesis (e.g., ferrihydrite, goethite, hematite), can limit pyrite precipitation—a significant sink for S and Fe (e.g., Berner, 1982; Berner and Raiswell, 1983). Since Fe is a redox-sensitive element, its sources and sinks vary among geochemical settings (Canfield, 1989; Canfield et al., 1992; Poulton et al., 2004). Consequently, Fe speciation by chemical extraction is a framework upon which Fe-based paleo-proxies have been developed to reconstruct oceanic paleoredox conditions (e.g., Lyons et al., 2009, and references reviewed in Raiswell et al., 2018). The term "highly reactive iron" (Fe_{HR}), defined here as the sum of Fe present as carbonates, oxides, magnetite, acid volatile sulfides (AVS), and pyrite (as defined by Poulton and Canfield, 2005), has been used to study Fe enrichments in modern and ancient sediments (e.g., Johnston et al., 2010; Li et al., 2010; Hardisty et al., 2018). For example, ratios of highly reactive Fe to total Fe (Fe_{HR}/Fe_T) above 0.38 are found associated with anoxic bottom waters in modern marine settings (Raiswell et al., 2001, 2018). In applications to ancient systems, high Fe_{HR}/Fe_T ratios coupled with low associated Fe_{Py}/Fe_{HR} ratios (<0.7) are attributed to ferruginous bottom waters, whereas high Fe_{Py}/Fe_{HR} ratios ($\geq$0.8) point to euxinic (sulfidic) conditions (Poulton and Canfield, 2011). However, recent studies (e.g., Raven et al., 2016; Scholz, 2018; Scholz et al., 2019) suggest that the interpretation of these proxies in continental margins can differ because of differences in geochemical factors, such as basin geometry, that affect Fe mobilization and deposition.

Sedimentary pyrite abundance is mainly controlled by the reactivity of organic matter, microbial sulfate reduction rate, and availability of Fe that can react with sulfide (Jørgensen, 1982; Berner, 1984; Fossing and Jørgensen, 1989; Jørgensen et al., 1990; Lyons, 1997). In marine sediments, pyrite formation is also a function of how spatially available Fe and S redox reactions are (Rickard and Luther, 2007). Moreover, sedimentary pyrite abundance has been widely used as a paleoredox proxy (Raiswell and Berner, 1985; Raiswell et al., 1994; Henderson, 2002; Large et al., 2014; Gregory et al., 2017; Sack et al., 2018). An important utility of pyrite as a proxy resides with the observation that in nonmarine settings, sulfate is generally the limiting reactant in pyrite formation, while Fe is generally limiting in marine settings (Raiswell and Berner, 1985; Raiswell et al., 1994; Raiswell and Canfield, 1998). However, recent studies (e.g., Riedinger et al., 2017) including this one reveal exceptions to this generalization.

The Santa Monica Basin (SMB), our chosen study site, is a confined inner basin within the California Continental Borderland where restricted deep-water ventilation leads to hypoxic bottom waters at its greatest depths (~900 m). The laminated (non-bioturbated) sediments in this basin are ideal for investigating biogeochemical parameters at high resolution (Gorsline, 1992; Kemnitz et al., 2020). Thus, this continental margin basin is an excellent location to study how terrigenous input, sediment transport, and bottom water chemistry affect the sediment biogeochemical cycle in a semi-restricted basin. To address our objective, we generated geochemical data on solid-phase and porewater samples from the upper sediment layers (up to 32 cm deep) from the basin and supplemented those results with a shelf-to-basin transect from 71 to 907 m water depth that comprises a transition from oxygenated (>60 μM O_2) to near-anoxic (~4 μM O_2) conditions. The geochemical data of the sediments from the basin are further scrutinized by means of reactive transport modeling. This model-data comparison yields detailed insight into the coupled cycling of C, Fe, and S and allows for quantitative rate estimates for organic matter remineralization and the associated cycling of Fe and S in the Santa Monica Basin sediments.

2. Material and Methods

2.1. Sampling

Sampling was conducted in May and July 2016 during single-day trips with the R/V Yellowfin operated by the Southern California Marine Institute. Dissolved O_2 concentrations were measured in the water column (190–907 m water depth) in May 2016 using a CTD (Sea-Bird 25) with an attached SBE43 oxygen sensor. Sediment samples were collected in July using a miniature multicorer (MUC, K.U.M. Kiel) equipped with four polycarbonate core liners (inner diameter 10 cm). To document the terrigenous input of sedimentation into the basin, we selected a depth transect of six stations extending from the shelf break, down the slope, to the basin plain (71 m to 907 m water depth; MUC-4 to −9), as well as an additional site located east of the transect at 893 m water depth (MUC-10). Sampling station details are provided in Fig. 1 and Table 1.

2.2. Sediment sampling

Sediment cores were processed in a cold room (4 °C). Cores were sliced inside a glove box under a constant flow of argon to minimize oxidation of oxygen-sensitive solutes. One core per station served for porewater extraction, a replicate core was collected for sediment solid-phase samples. Sediments were sliced in 1-cm increments between 0 and 10 cm, in 2-cm increments between 10 and 20 cm, and in 4-cm increments below 20 cm. Sediments were transferred to argon-flushed 50 mL conical tubes and frozen at −30 °C. For porewater extraction, sediments inside conical tubes were centrifuged at 4300 × g for 20 mins to separate the porewater from the sediment.

2.3. Porewater analyses

Porewater was immediately analyzed for dissolved sulfide according to Cline (1969; detection limit 3 μM) and iron (II) according to Kremling et al. (1999; detection limit ~ 20 nM). Although the Cline method reported a sulfide detection limit by the photometric method of ~ 3 μM, we feel comfortable reporting lower sulfide values because our concentration standards showed a linear correlation with absorbance down to 0.8 μM. Concentrations of the solutes were determined with a Shimadzu UV-Spectrophotometer (UV-1800) equipped with a sipper unit. The remaining porewater was collected into plastic vials, stored at 4 °C, and later analyzed for sulfate using an ion chromatograph (Metrohm 761). Sulfate samples were pre-filtered through a 0.2 μm AcroDisk filter prior to analyses. Based on repeated analysis of IAPSO seawater standards, analytical precision of sulfate

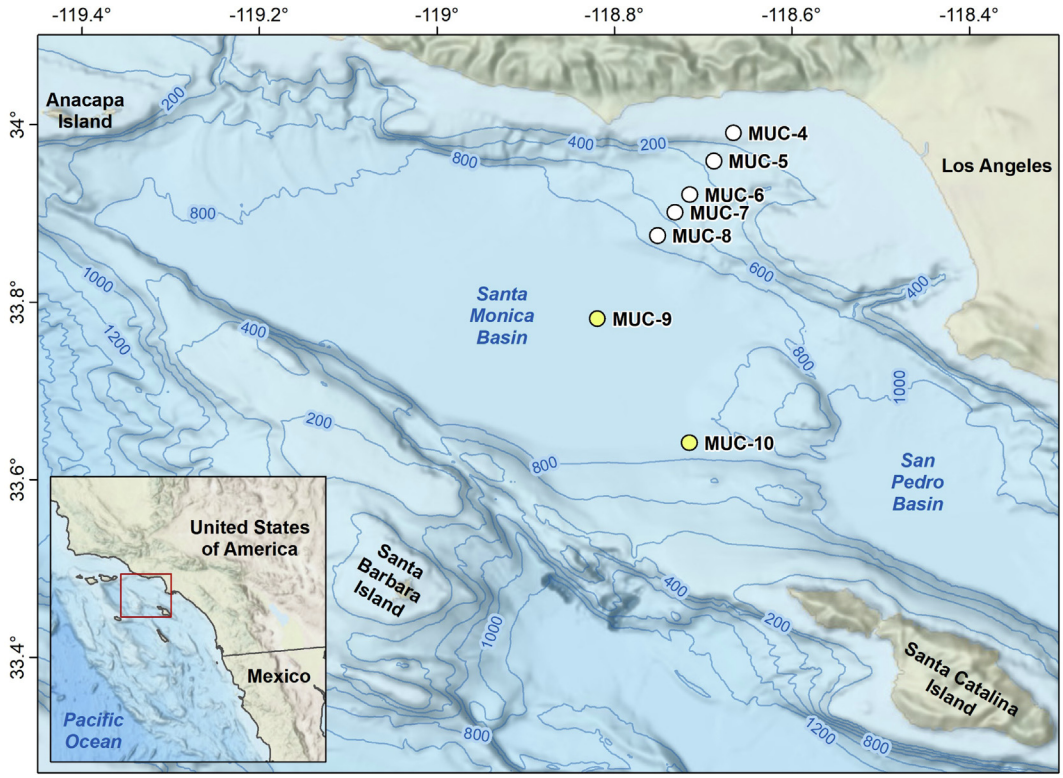

Fig. 1. Bathymetric map of the Santa Monica Basin with sampling station locations. The stations from the basin (marked in yellow) are the main focus of this paper.

Table 1
Station data. MUC = multicorer station, CTD = CTD station, n.d. = not determined, O_2 bottom water = oxygen concentration in water ca. 2–5 m above seafloor.

Instrument ID	Depth (m)	O_2 bottom water (μM)	Latitude (N)	Longitude (W)	Date
MUC-4	71	n.d.	33°59.443	118°39.967	13–07-2016
MUC-5	319	n.d.	33°57.570	118°41.144	13–07-2016
MUC-6	485	n.d.	33°55.342	118°42.747	13–07-2016
MUC-7	537	n.d.	33°54.126	118°43.646	21–07-2016
MUC-8	695	n.d.	33°52.440	118°44.950	21–07-2016
MUC-9	907	n.d.	33°46.677	118°49.067	21–07-2016
MUC-10	893	n.d.	33°38.648	118°42.735	27–07-2016
CTD-1	907	4.4	33°45.948	118°49.751	24–05-2016
CTD-2	785	5.6	33°51.669	118°45.615	24–05-2016
CTD-3	540	14.5	33°54.070	118°43.911	24–05-2016
CTD-4	411	31.7	33°56.483	118°42.007	24–05-2016
CTD-5	190	61.1	33°58.545	118°40.460	24–05-2016

was < 1 %. The absolute detection limit of sulfate was 1 μM, which corresponds to 30 μM in the undiluted sample.

2.4. Solid-phase geochemical analyses

An ELTRA CS500 carbon–sulfur analyzer was used to quantify total organic carbon (TOC) from dried and homogenized sediments, which allows measurement of total carbon by combustion and total inorganic carbon via hot (80 °C) hydrochloric acid treatment. TOC was determined by difference between total carbon and total inorganic carbon. Acid volatile sulfides (AVS) were extracted under a N_2 atmosphere using freshly thawed frozen samples and a 6 N HCl-stannous chloride solution for 45 min. The liberated sulfur flows into a silver nitrate trap solution (3 % $AgNO_3$, 10 % NH_4OH) where it precipitates as Ag_2S. Following the AVS extraction, the remaining sediment residue was filtered through a 0.45 μm filter membrane. The filters were then boiled under an acid $CrCl_2$ solution for 2 h to extract S held in pyrite and determine pyrite (FeS_2) content (chromium reducible sulfur [CRS] method; Canfield et al., 1986). The liberated sulfur, captured as Ag_2S, was filtered through a 0.45 μm cellulose (MF-Millipore) membrane filter. The filtered Ag_2S precipitates were dried and weighed for gravimetric determinations of AVS and pyrite contents and were subsequently used for sulfur isotope analysis.

Iron speciation was undertaken using a modified version of the sequential iron extraction from Hardisty et al. (2016) and Raiswell et al. (2018). Frozen sediments were thawed while remaining sealed in 50 mL centrifuge tubes with N_2 flushed headspeace to avoid exposure to air; 100 mg of each sample were used to perform the extractions. The extraction sequence began with an ascorbic acid step targeting ferrihydrites, Fe_{asc}, the most labile ferric phases and first poorly-ordered Fe oxyhydroxide phase precipitated from Fe^{2+} oxidation (Raiswell et al., 2010). Additional steps used sodium acetate to extract Fe-carbonates, Fe_{ace}; sodium dithionite to extract crystalline (oxyhydr)oxides, such as lepidocrite, goethite, and hematite, Fe_{dith}; and ammonium oxalate to extract magnetite, Fe_{ox} (Poulton and Canfield, 2005; Raiswell et al., 2018). Importantly, sequential iron extractions were performed only a few days after

sample collection to avoid oxidation of reactive Fe-sulfide phases. To minimize oxidation of iron sulfide phases, the solutions were bubbled with N_2 prior to extraction, and the vials were filled with N_2 and sealed during each chemical step. The iron concentration in each solution was analyzed by ICP-MS (Agilent 7500c) after dilution in 2 % trace metal grade HNO_3. Replicate samples yielded precisions of < 4 % for all extractions. Iron present as AVS and pyrite were calculated from measured values of AVS-S and pyrite-S assuming FeS and FeS_2 stoichiometries, respectively. Highly reactive Fe (Fe_{HR}) was then calculated from the analyzed iron phases using the definition in Poulton and Canfield (2005) and Raiswell et al. (2018), where Fe_{HR} is defined as the sum of Fe_{asc} + Fe_{dith} + Fe_{ace} + Fe_{ox} + Fe_{AVS} + Fe_{py}. Any concerns about Fe present as AVS being extracted during the sequential Fe steps is mitigated by the very low amounts of AVS present.

Bulk concentrations of Fe and Al were determined by ICP-MS analysis following multi-acid total digestion. Approximately 100 mg of dried, homogenized powders were combusted at 450 °C for 12 h to remove any combustible carbon and sulfides. The remaining sample splits were dissolved in trace metal grade HCl:HNO_3:HF and analyzed using an Agilent 7900 Inductively Coupled Plasma Mass Spectrometry (ICP-MS) at the University of California, Riverside (UCR). The accuracy and the precision of the measurements were verified using certified reference materials USGS SGR0-1b and NIST 2702 with replicates (n = 9) and found to be within 3 % of expected values.

2.5. Mössbauer spectroscopy

Mössbauer spectroscopic measurements (MBS) were carried out to gain insights into the nature of different Fe species, such as different Fe-oxide mineralogies, Fe-carbonates (e.g., siderite), and Fe-sulfides, as well as to identify different pools of ferrihydrite-organic matter complexes that are otherwise difficult to characterize unambiguously by chemical extractions and other spectroscopic techniques (e.g., XRD, Fe-EXAFS). Characterizations via Mössbauer spectroscopy for the top and bottom sediments of MUC-7 and MUC-9 were undertaken at multiple temperatures, at room temperature (RT), 225 K, 77 K, 35 K and 12 K, to gain additional insight into variations in Fe speciation and mineralogy as a function of redox conditions. Mössbauer measurements were performed at the Environmental Molecular Science Laboratory (EMSL) at Pacific Northwest National Laboratory. The variable temperature ^{57}Fe-Mössbauer spectroscopy (MBS) was undertaken using a WissEl Elektronik and a Web Research instrument that included a closed-cycle cryostat SHI0850, a Sumitomo CKW-21 He compressor unit, and an Ar-Kr proportional counter detector. The MBS data were modeled using a Voigt-based hyperfine distribution model (Rancourt and Ping, 1991). The samples were immediately stored in anoxic environmental chamber with oxygen levels below 0.5 ppm until sample preparation, following the routine procedures reported in (Peretyazhko et al., 2012). The samples were then inserted into the Mössbauer with minimum exposure time. See the Supplementary Material for a detailed description of this procedure.

2.6. Stable Isotopes

For the isotopic composition of organic carbon and nitrogen, first the sediment sample splits were acidified with 0.2 N HCl to remove inorganic carbon and subsequently dried at 60 °C to remove the HCl. Atomic ratios of organic C to total N (C_{org}/N_T) and their stable isotopes were then measured using a Costech ECS 4010 Analyzer – Delta V Plus Isotope Ratio Mass Spectrometry (IRMS). The isotopic ratios are given in delta notation relative to Vienna Pee Dee Belemnite (VPDB) for $\delta^{13}C$ values and relative to air for $\delta^{15}N$ values. Glycene, peach, acetate, and house soil were used as reference material. Standard error (1σ) was < 0.40 ‰ for $\delta^{15}N$ and < 0.10 ‰ for $\delta^{13}C$. C/N ratios showed an accuracy of 0.2 % relative to standard reference materials.

For determination of the sulfur isotope compositions of AVS and pyrite, the Ag_2S recovered during those extraction steps was combusted with a Costech elemental analyzer connected via continuous helium flow to a Delta V Plus IRMS. Sulfur isotope measurements were calibrated with reference materials IAEA-S0-6 and sulfanilamide standard, with standard error (1σ) of < 0.09 ‰ for $\delta^{34}S$.

2.7. Radiocarbon

Radiocarbon values were measured to interpret the reactivity of the organic carbon by using accelerator mass spectrometry (AMS) at the University of California, Irvine, (UCI) Keck Carbon Cycle Accelerator Mass Spectrometry (KCCAMS) laboratory. Core-top sediments (0–1 cm depth) from the shelf (MUC-4), the slope (MUC-6), the base of the slope (MUC-8), and the basin (MUC-9 and −10) were selected for comparison. For the basin, additional sediment samples from multiple depths were also measured. Samples were exposed to HCl vapor for 4 h to remove calcium carbonate, dried on a vacuum line, combusted, graphitized, and then counted on the AMS. Sample preparation backgrounds were subtracted based on measurements of acidified glycine, sucrose, and lysine. Radiocarbon results were corrected for isotopic fractionation according to the conventions of Stuiver and Polach (1977), with $\delta^{13}C$ values measured on prepared graphite using the AMS spectrometer.

Radiocarbon calibration for age correction was made using the OxCal 4.3 software (Ramsey, 2009), integrating the IntCal13 and Marine13 Radiocarbon Age Calibration Curves from Reimer et al. (2013) and the Bomb13NH1 Bomb Series curve from Hua et al. (2013). Further age adjustment was made with a reservoir age of 270 ± 55 as established by Ingram and Southon (1996) for total organic carbon from the California Borderland sediments.

2.8. Reactive-Transport Model

The goal of the biogeochemical model was to aid in the quantitative interpretation of the primary porewater and solid-phase constituents of the SMB sediments. To this end, we chose a parsimonious reaction set, which was tailored to the collected data. Our model does not include nitrogen, manganese, or methane cycles because we lack the data to validate the model fully, which could lead to over-fitting of the model to the data. This approach implies that omitted reactions will be lumped with other reaction rates. For example, iron oxidation with nitrate will be included in aerobic iron oxidation. We calibrated the model using the vertical sedimentary profiles of POC, dissolved sulfate, dissolved iron, and dissolved sulfide. The initial purpose of the reaction-transport model was the derivation of reaction rates and benthic fluxes. The second goal of the model was to mechanistically evaluate the primary environmental controls of iron cycling in basinal SMB sediments.

We included twelve state variables: the concentrations of highly reactive, moderately reactive, and unreactive organic matter ([CH_2O_{HR}], [CH_2O_{MR}], [CH_2O_U]); bicarbonate ([HCO_3^-]); ammonium ([NH_4^+]); oxygen ([O_2]); reactive iron oxide ([$FeOOH_R$]); unreactive iron oxide ([$FeOOH_U$]); dissolved ferrous iron ([Fe^{2+}]); sulfate ([SO_4^{2-}]); total dissolved sulfide ([ΣH_2S]); and pyrite ([FeS_2]). The reaction set consisted of eleven reactions. Both highly reactive and moderately reactive organic matter are oxidized by O_2 (aerobic respiration), $FeOOH_R$ (dissimilatory Fe[III] reduction), and SO_4^{2-} (sulfate reduction). The sequence of terminal electron acceptors

is implemented using conventional inhibition-limitation formulas (Soetaert et al., 1996), which treat aerobic respiration as the dominant mineralization pathway in the presence of O_2; dissimilatory Fe(III) reduction and sulfate reduction become important when O_2 is depleted (Froelich et al., 1979). Both Fe^{2+} and ΣH_2S are oxidized with oxygen. Total dissolved sulfide is also oxidized by $FeOOH_R$ via sulfide-mediated Fe(III) reduction, while FeS_2 precipitates when Fe^{2+} and ΣH_2S are present in the porewater at the same time. Pyrite is oxidized in the presence of O_2. Transport occurs via molecular diffusion and advection (we did not include activity of benthic fauna, as there was no evidence for such activity during sampling). The model adopts a constant sediment accumulation rate of 0.10 g cm^{-2} yr^{-1} (Kemnitz et al., 2020), which was determined via core dating.

The model structure, set-up, and numerical solution procedure have been described elsewhere (i.e., van de Velde and Meysman, 2016; van de Velde et al., 2018; Oueslati et al., 2019). Briefly, the reaction-transport model consists of a set of mass-balance equations of the advection–diffusion-reaction form Boudreau (1996) and Meysman et al. (2005) that are implemented in the open-source language R. A steady-state solution is attained by following the step-by-step procedure outlined in Soetaert and Meysman (2012). The upper boundary conditions for dissolved constituents were set at fixed concentration, based on *in situ* measurements (Table S5). However, the upper boundary conditions for solid-phase species were set at 'fixed flux', also, calibrated on the *in situ* data. For all species, the lower boundary condition was set at 'no gradient', apart from SO_4^{2-} and Fe^{2+}, for which a clear downward gradient was present. For these species, we set the boundary condition at 'fixed flux'. Only two parameters were used to fit the model to the observed profiles:; the precipitation rate of FeS_2 (k_{PyP}) and the reoxidation of HS^- with FeOOH (k_{SMI}) (Figure S4). Further details about model parametrization can be found in the Supplementary Material.

Three model experiments were designed to evaluate the impact of changing bottom-water O_2 (O_{2BW}), POC flux, and reactive OM efficiency on dissolved Fe (DFe) inventory and benthic Fe flux. These model experiments were designed to illustrate the important environmental factors that determine whether a low-oxygen, unbioturbated sediment column becomes an iron dominated system. For each individual model experiment, all parameters and boundary conditions were kept at their baseline value, and the investigated boundary condition was varied from 0 – 400 μM (bottom-water O2), 0–14 mmol C m^{-2} d^{-1} (POC flux) or 0 – 1 (fraction of less reactive POC).

3. Results

3.1. Solid-phase sediment chemistry

The relationships among total organic carbon (TOC), highly reactive iron (Fe_{HR}), and FeS_2 content for the shelf, slope, and basin sediments are presented in Fig. 2. TOC concentrations were markedly lower in sediments collected from the oxygenated shelf and slope (depth-averaged concentration for the slope: 2.9 ± 0.9 wt.% C; for the shelf: 0.9 ± 0.1 wt.%C) compared to sediments collected from the basin (depth-averaged concentration: 4.15 ± 0.09 wt% C), in agreement with previous observations (i.e., Gorsline, 1992; Kemnitz et al., 2020). A conspicuous TOC depletion was observed at 14–17 cm depth in MUC-9 and 25–32 cm depth in MUC-10, which likely corresponds to turbidite deposits, as indicated by porosity measurements from the same MUC deployments (Kemnitz et al., 2020) and by previous field studies (Huh et al., 1987; Gorsline, 1996; Gorsline et al., 2000; Komada et al., 2013). Highly reactive Fe (Fe_{HR}) showed an enrichment at the sediment–water interface in the basin sediments (2.6–3.7 wt% Fe_{HR}; Fig. 2), whereas the slope sediments had lower Fe_{HR} (≤1.83 wt%). Both AVS and pyrite were unexpectedly low. The shelf, slope, and basin sediments host negligible amounts of AVS (≤0.03 wt% AVS), with concentrations in MUC-4 and MUC-10 mostly below detection limit (<10^{-3} wt% AVS); due to the scant amount of AVS detected, the data was not included in the plot. Pyrite concentrations from the shelf were below detection limit (<10^{-3} wt% CRS). Pyrite concentrations in the basin sediments (depth-averaged concentration: 0.11 ± 0.07 wt% FeS_2) were lower than those in the slope sediments (depth-averaged concentration: 0.35 ± 0.18 wt% FeS_2).

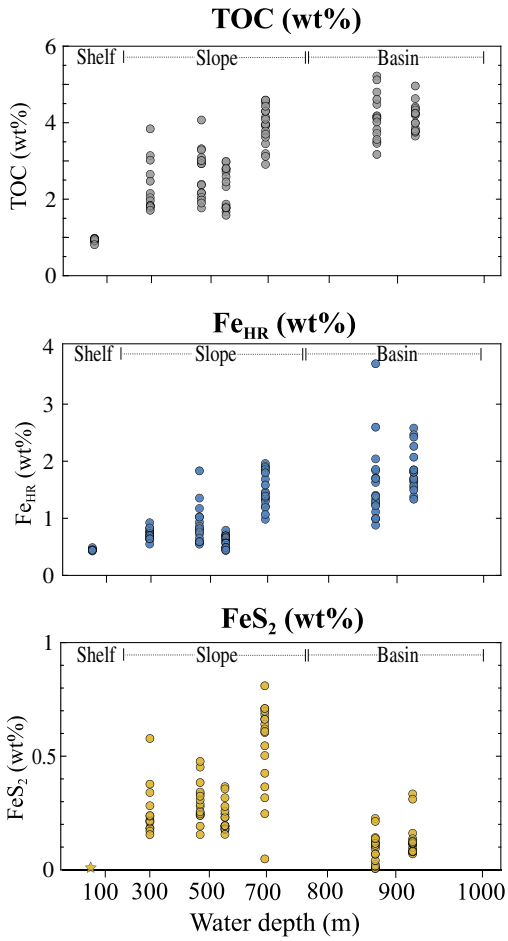

Fig. 2. Solid-phase concentration profiles of (a) total organic carbon (TOC), (b) highly reactive iron (Fe_{HR}), and (c) pyrite content from all sediment core stations. The yellow star represents samples that were below the detection limit.

3.1.1. Stable sulfur isotope values

Sulfur isotope data for pyrite ($\delta^{34}S_{py}$) are shown in Fig. 3. As a consequence of low AVS and pyrite concentrations, $\delta^{34}S$ measurements for AVS were not possible, while $\delta^{34}S_{py}$ measurements were only possible from the slope sediments (MUC-5, −6, −7) and from specific depths of the basin sediments (MUC-9 and −10). In the slope sediments, $\delta^{34}S_{py}$ values for the surface are enriched in ^{34}S relative to the underlying pyrite ($\delta^{34}S_{py}$ from −36.0 ‰ to −43.9 ‰ respectively). The underlying sediments, by contrast, show stronger ^{34}S depletions as a consequence of favorable microbial sulfate reduction under more reduced porewater conditions. In the sediments from the basin, the $\delta\ ^{34}S_{py}$ are overall heavier relative to the slope (from −33.9 ‰ to −22.4 ‰) as a probable result of closed system pyrite formation.

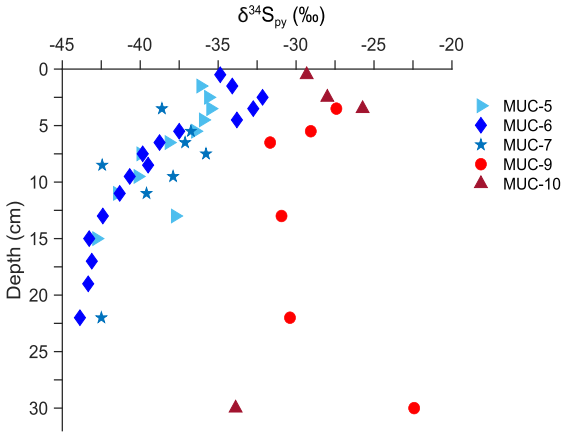

Fig. 3. Sulfur stable isotope profiles from pyrite ($\delta^{34}S_{py}$) derived from the CRS extraction. Reported in delta notation relative to Vienna-Cañon Diablo Toilite (VCDT).

3.1.2. Iron speciation

Fig. 4 shows the relationship between highly reactive Fe and pyrite formation using the Fe_{HR}/Fe_T and Fe_{py}/Fe_{HR} ratios. The shelf profile lacks the Fe_{py}/Fe_{HR} ratios due to pyrite being below detection limit. The slope profiles (MUC-5, 6, 7, and 8) show that Fe_{py}/Fe_{HR} increases as Fe_{HR}/Fe_T decreases, indicative of efficient Fe (oxyhydr)oxides (hereafter referred to as FeOOH) reduction and Fe sulfidization. However, Fe_{py}/Fe_{HR} from the basin (MUC-9 and −10) is remarkably low (mean Fe_{py}/Fe_{HR} ratio = 0.04 ± 0.02), indicating a lack of pyrite formation. Moreover, the slope sediments contain higher Fe_{py}/Fe_{HR} ratios (up to 0.43), meaning more Fe sulfidization is occurring in the slope than in the basin.

The surface sediments from the basin have Fe_{HR}/Fe_T ratios (0.54 MUC-9 and 0.64 MUC-10) much higher than the 0.38 threshold that typically defines the boundary between oxic and anoxic sediments (Raiswell et al., 2001, 2018). These values are similar to those from the modern euxinic Cariaco Basin (0.51 ± 0.03) and Black Sea (0.70 ± 0.19) (Raiswell and Canfield, 1998; Anderson and Raiswell, 2004). However, from the iron speciation data (see Fig. 5) we observe that our elevated Fe_{HR}/Fe_T ratios correspond mainly to the enrichment of FeOOH rather than enrichments of reduced Fe phases, as is the case for euxinic systems.

We focus our observations of Fe speciation on the sediments from the deeper basin (MUC-9 and MUC-10; Fig. 5). An interesting relationship is the elevated enrichment of ferrihydrite in the surface sediment, with 1.36 wt% Fe_{asc} (28.4 % of total Fe) for MUC-9 and 1.41 wt% Fe_{asc} (24.1 % of total Fe) for MUC-10. This enrichment is also evident in the exceptionally elevated Fe/Al ratios (0.8 and 1.1) within the surface sediments. Additionally, Kemnitz et al. (2020) reported a light reddish-brown color for the first centimeter of the surface sediment of MUC-9 and −10, in agreement with notable enrichment in iron oxides. The FeOOH of more crystalline phases (hematite and geothite; Fe_{dith}) remained high even well below the sediment–water interface (with depth-averaged values of 18.2 ± 3.2 % and 11.6 ± 3.8 % of the total Fe for MUC-9 and −10, respectively). Magnetite (Fe_{ox}) and Fe(II)-carbonate (Fe_{ace}), both containing unsulfurized Fe^{2+}, were detected but in lesser amounts than Fe_{dith}.

Our Fe speciation is in strong agreement with the Fe speciation performed by Burdige and Komada (2020) from an adjacent site in SMB. Additionally, they found remarkably high amounts of poorly reactive Fe sheet silicates corresponding to 42 ± 22 % of total Fe in the surface sediments (0–1 cm) and 58 ± 18 % of total Fe below the surface (3–20 cm; Burdige and Komada, 2020). Our poorly reactive fraction (calculated as $Fe_{PR} = Fe_T - Fe_{HR}$) is consistent with the Fe sheet silicate content reported by Burdige and Komada (2020), present as 42.4 % of total Fe in the surface sediments (0–1 cm) and 60.5 ± 6.2 % of total Fe below the surface (3–20 cm). Usually, in continental margin sediments, Fe sheet silicates correspond to about 23 % of total Fe (Raiswell and Canfield, 1998).

3.1.3. Mössbauer spectroscopy

Mössbauer spectroscopic (MBS) measurements were carried out on slope sediments (MUC-7, 537 m) and basin sediments (MUC-9, 907 m), specifically the sediment surface (0–1 cm) and the bottom of the sediment core (20–24 cm and 28–32 cm respectively), in order to determine the variation in Fe species and to identify different pools of ferrihydrite-OM complexes. The main purpose for our MBS effort was to further characterize the Fe mineralogy of the basin sediments and contrast the findings with MBS data from the slope sediments.

A comparison of Fe mineral phases from sequential Fe extraction and MBS detection from the basin sediments is detailed in Table 2. For a more quantitative description of the MBS Fe phases detected see Table S1 for the basin sediments, and Table S2 for the slope sediments. For all samples, we detected crystalline Fe-oxides such as 'large particle' (>50 nm) hematite and magnetite (Goya et al., 2003; Murad and Cashion, 2004), Al-substituted goethite (Steve and Fysh, 1982), <50 nm magnetite (Goya et al., 2003), poorly-crystalline ferrihydrite-like coprecipitates (Chen et al., 2015; Zhao et al., 2020), epidote, siderite (Peretyazhko et al., 2012), and Fe-containing silicates, but pure ferrihydrite features were absent. The amount and type of ferrihydrite-like mineral phases, however, differed significantly between the samples.

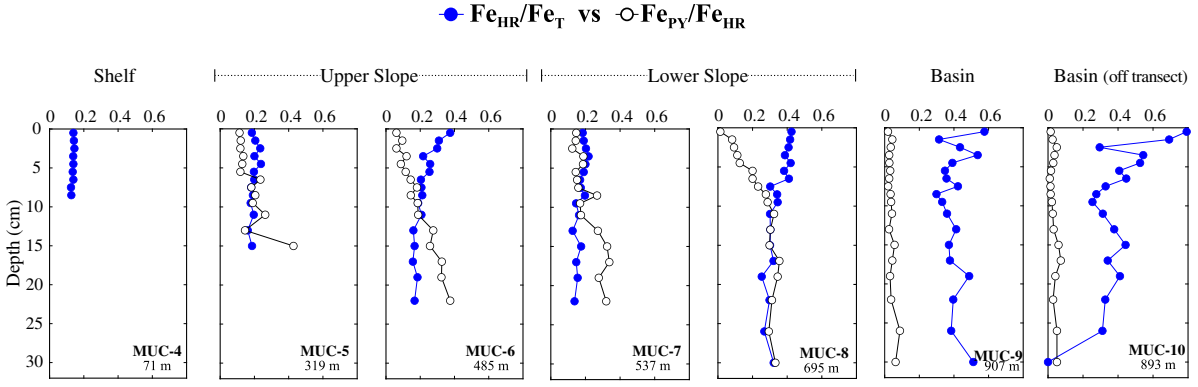

Fig. 4. Fe_{HR}/Fe_T and Fe_{Py}/Fe_{HR} profiles representing the relationship between highly reactive Fe and pyrite.

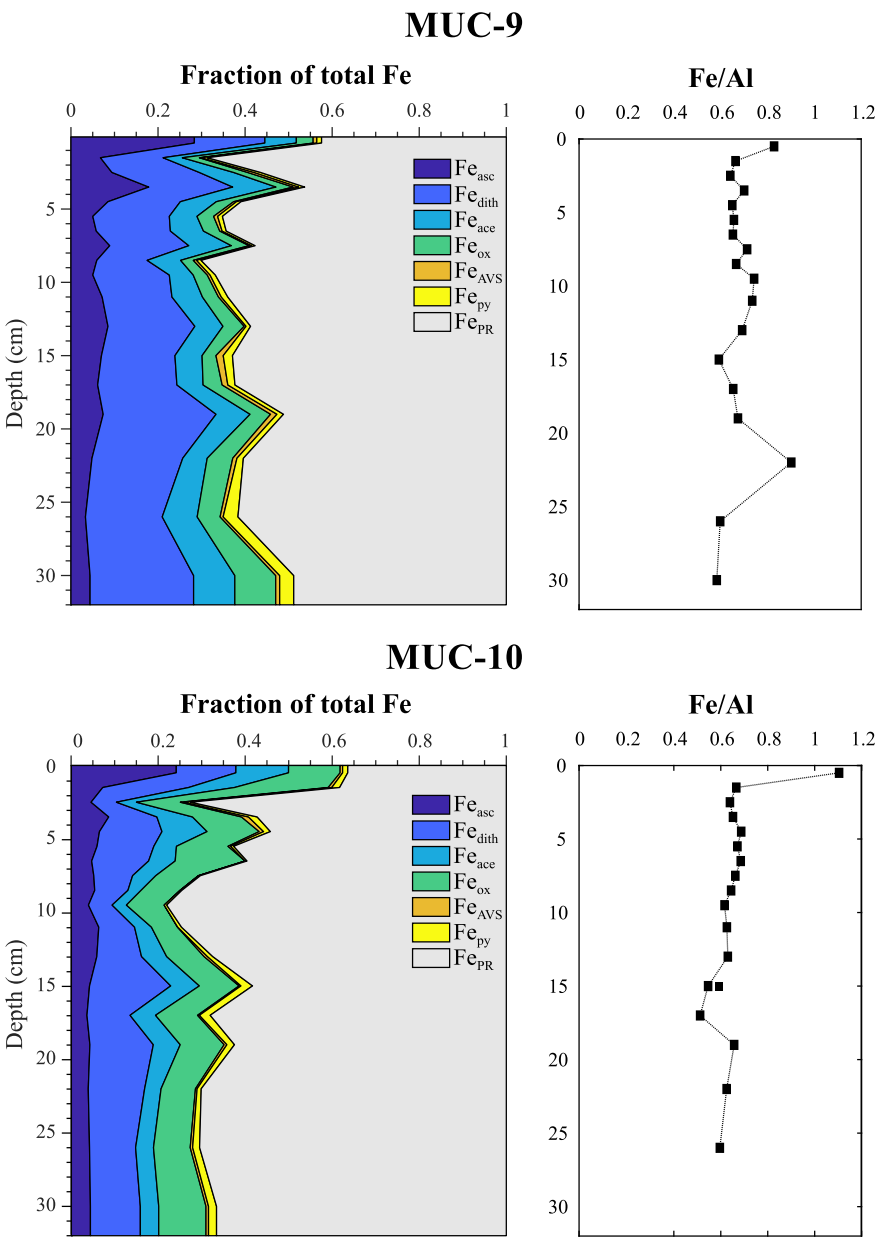

Fig. 5. Solid-phase iron speciation profiles. The Fe species appear from left to right. Leftmost is the labile Fe oxides (e.g. amorphous ferrihydrite) from the Fe_{asc} extraction, followed by crystalline Fe oxides (e.g. goethite, hematite) from the Fe_{dith} extraction, followed by magnetite from the Fe_{ox} extraction, then Fe(II)-Carbonates from the Fe_{ace} extraction, following Fe-pyrite from the chromium reduction extraction, and on the rightmost side is Fe-AVS from the AVS extraction. The solid line is total iron (Fe_T). On the right, Fe/Al ratio from sites (A,B) MUC-9 and (C,D) MUC-10.

The samples from the basin contain two spectral features indicative of a ferrihydrite-like phase coprecipitated with organic matter (Fe(III)-OM-1 and Fe(III)-OM-2, Fig. 6). The presumed Fe (III)-OM-1 spectrum is a well-defined sextet spectral feature that corresponds well with ferrihydrite-OM coprecipitates (e.g., Chen et al., 2015). The presumed Fe(III)-OM-2 spectral feature is similar to one observed in grassland soils (Zhao et al., 2020) that was attributed to ferrihydrite-OM coprecipitates. However, the hyperfine fields in Zhao et al. (2020) were higher on average (|H| = 25–30 T) than in our samples (|H| ≈ 20 T); therefore, we speculate that Fe(III)-OM-2 corresponds to a Fe(III)-OM pool with higher OM/Fe ratios relative to Fe(III)-OM-1 and the ferrihydrite-OM noted in Zhao et al. (2020). The Mössbauer spectra for MUC-7 do not show the spectral features attributed to ferrihydrite-OM coprecipitates (see Fig. 6).

For the basin sediments, both Fe(III)-OM-1 and Fe(III)-OM-2 features were detected in the top sediments; however, Fe(III)-OM-1 was absent in the bottom sediment. Fe(III)-OM-2 was detected with a decrease from 18.6 % to 11.9 % of total Fe, although it remained higher than Fe_{asc} values from the sequential Fe extraction (4.4 % of Fe_T). These observations lead us to suggest that Fe (III)-OM-2 is a more crystalline phase and may be associated with the crystalline Fe (oxyhydr)oxide phases quantified with the Fe_{dith} extraction. However, additional studies are needed for precise identification of this Fe(III) phase. In addition to OM, Si could be associated with the poorly crystalline Fe-oxide precipitated. However, the MBS feature for co-precipitated Si is a well-defined sextet at 12 K (Zhao et al., 1996), whereas our samples produce a sextet at 12 K that is associated with goethite given their parameters and relative content agree with the goethite spectra feature present

Table 2
Iron mineral phases in sediments and methods for determination of Fe mineralogy. Below MBS detection, P corresponds to *present phase*, and A corresponds to *absent phase*. For more details on the quantitative portion of the MBS detection, see Supplementary Material Tables S1 and S2.

Iron mineral phase	Fe from sequential extraction (% of Fe_T)		MBS detection		MBS description
	Top (0–1 cm)	Bottom (28–32 cm)	Top (0–1 cm)	Bottom (28–32 cm)	
Amorphous, poorly crystalline Fe oxyhydroxides (e.g. ferrihydrite) *{Fe_{ac}}*	28.4	4.4	P	A	Top: Fe(III)-OM-1 and Fe(III)-OM-2 make up ~ 1/3 of total Fe. Bottom: Fe(III)-OM-1 is absent or incospicuous. Some of the Fe(III)-OM-2 could be ferrihydrite.
More crystalline Fe oxides (e.g. goethite, hematite) *{Fe_{dith}}*	16.2	23.8	P	P	Goethite, hematite and Fe(III)-OM-2 content in agreement with Fe_{dith} content at both depths.
Fe(II)-Carbonates (e.g. siderite) *{Fe_{ace}}*	7.2	9.5	P	P	Present in less concentration than the Fe_{ace} extraction Top: Siderite ≈ 3.5 % of total Fe. Bottom: Siderite ≈ 4.2 % of total Fe.
Magnetite *{Fe_{ox}}*	3.9	9.4	P	P	Top: In agreement with Fe_{ox} content. Bottom: Only a small amount of nano-magnetite detected.
Structural Fe silicates and refractory iron minerals (e.g.chlorite, mica, feldspar, amorphous silicates, epidote)	57.6	51.2	P	P	Top: In agreement with Fe_{PR} extraction. Bottom: The fraction of silicates and refractory iron minerals accounts for ~ 2/3 of the total Fe.
	Fe from CRS extraction				
Pyrite (FeS_2) *{Fe_{py}}*	1.1	3.2	P	P	Small amount of pyrite at both depths, in agreement with CRS content.
	Fe from AVS extraction				
Fe-monosulfide (e.g. mackinawite) *{Fe_{AVS}}*	0.8	0.9	A	A	Absent or inconspicuous.

For MBS detection, P corresponds to *present* Fe phase and A corresponds to *absent* Fe phase. A complete description on the quantitative portion of the MBS detection is available under Supplementary Materials.

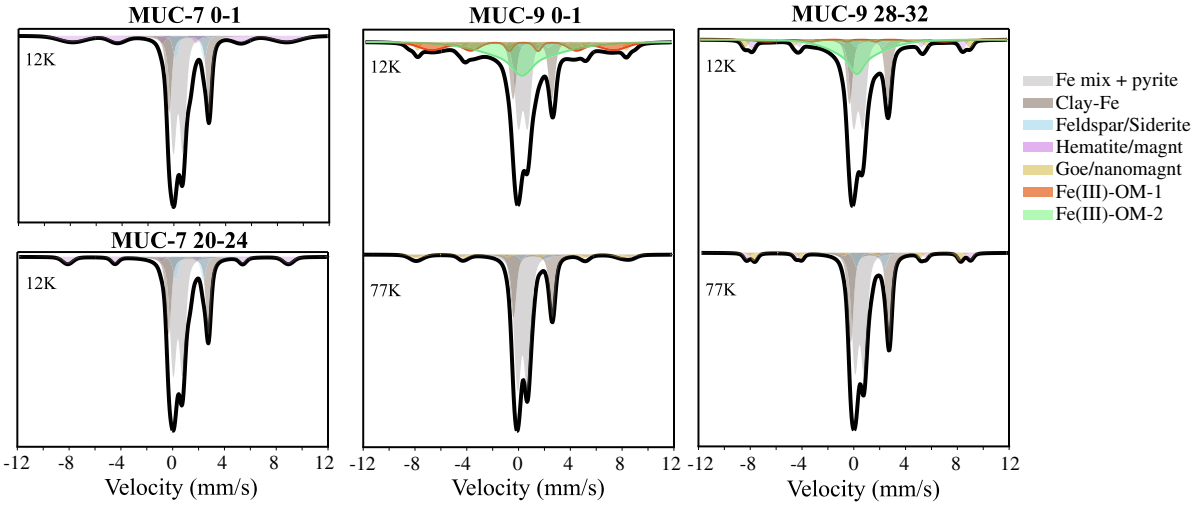

Fig. 6. Mössbauer variable temperature spectra (77 K – 12 K) for the sediment samples from the basin (MUC-9; 0–1 cm and 28–32 cm depth) and one temperature spectra at 12 K for the slope sediments (MUC-7; 0–1 cm and 20–24 cm depth). The different colors correspond to different spectra features, see the legend for identification of Fe phases. Notice the identifiable presence of two types of Fe(III)-coprecipitates at 12 K for the basin (MUC-9) yet absent in the slope sediments (MUC-7). Magnt, magnetite; Goe, goethite.

at 77 K. Goethite and hematite were detected in both the top (~4% of total Fe) and bottom (~6% of total Fe) sediments but in amounts less than those detected by the Fe_{dith} extraction (16.2 % of Fe_T and 23.8 % of Fe_T, respectively), consistent with the assumption that Fe (III)-OM-2 belongs to a crystalline Fe (oxyhydr)oxide phase, and that the Fe_{dith} extraction may extract this Fe species.

The presence of siderite is unambiguous (Table 2) but in relatively small amounts (top ≈ 3.5 % of total Fe; bottom ≈ 4.2 % of total Fe). These results confirm that the Fe_{ace} step is extracting Fe (II)-carbonates from modern marine sediments; however, the relatively high Fe_{ace} content may indicate that additional species are being extracted during this extraction step. Magnetite is present in lower amounts (relative to Fe_{ox}) as nano-magnetite, suggesting that the Fe_{ox} step may be extracting additional Fe phases, such as clay minerals (e.g., nontronite) as noted in recent work of Hepburn et al. (2020). Finally, a large fraction of the Fe is sequestered as Fe(II) and Fe(III) in silicate minerals (top ≈ 50 % of total Fe; bottom ≈ 60 % of total Fe). Since the silicate mineral distribution is complex, we are not able to precisely identify individual contributions of these minerals in the spectra, but it is consistent with our poorly reactive Fe fraction. In addition to silicate minerals, Fe sequestered in epidote is also evident. Small amounts of pyrite (~2% total Fe) were also detected, consistent with results from the CRS extractions. However, no mackinawite nor any other Fe-monosulfide phase was detected, suggesting that the AVS fraction might be in dissolved phase, in accordance with Rickard and Morse (2005) or that any FeS in the sediment could have been chemically altered during sample handling, although the risk of the latter is minimized by the very short sample exposure to air during sample extraction and/or processing for MBS analyses.

3.2. Sediment porewater

The porewater Fe^{2+} concentrations for all the sediment cores are plotted in Fig. 7. Additionally, the Fe^{2+} concentrations for core-tops (0–1 cm) and the overlying water for all stations are reported in Table 3. The Fe^{2+} content from the top sediment layer increased from 6.3 μM Fe^{2+} in the shelf sediments to 131.1 μM Fe^{2+} in the deep basin sediments. However, the highest Fe^{2+} content came from the off-transect basin station (MUC-10) at 155.9 μM Fe^{2+}. From the overlying waters, Fe^{2+} was below detection from the shelf (MUC-4) to mid-slope (MUC-7), where bottom waters consist of > 10 μM O_2. At greater water depth and the associated decrease in O_2 (5.6 – 4.4 μM O_2), we observed quantifiable Fe^{2+} with the highest values measured from the deepest station in the basin (0.9 μM Fe^{2+}; MUC-9). The concentration gradient of dissolved Fe between the bottom water and uppermost porewater was used to calculate the diffusive benthic flux across the sediment–water interface (Table 3). The calculated benthic Fe fluxes from the uppermost sediments from all stations indicate release of Fe^{2+} to the water column. The benthic efflux of Fe from the shelf and slope sediments are further supported by elevated TOC delivery and evidence for benthic macrofauna (see Kermnitz et al., 2020, for macrofauna description).

The measured porewater H_2S values were overall below detection limit for the shelf and slope sediments and close to the detection limit for the basin (2.6 ± 0.5 μM H_2S, MUC-9). See Section 3.3.1 for further details on sulfide content from the basin sediments.

3.3. Organic matter source

To further investigate if reactive organic matter is a limiting factor in iron sulfide precipitation, we assessed the source(s) of organic matter (OM) found in the slope and basin using geochemical tracers. Fig. 8 shows the relationship between C_{org}/N and $\delta^{13}C_{org}$, revealing a clear distinction between shelf/slope and basin sediments. For the shelf and slope, mean C_{org}/N ratio of 14.1 ± 1.1 and mean $\delta^{13}C$ value of −24.4 ± 0.9 ‰ were observed. In contrast, the basin has lower C_{org}/N ratios of 11.3 ± 0.5 and slightly heavier $\delta^{13}C$, with mean values of −21.9 ± 1.1 ‰. The turbidite layers show a distinctly different signal compared to both slope and basin sediments, with overall higher C_{org}/N ratios and much lighter $\delta^{13}C$ values (Fig. 8). The shelf and slope sediments have a high average C_{org}/N ratio, indicative of high input of terrestrial organic matter (Lamb et al., 2006); however, the $\delta^{13}C$ values are slightly heavier than the common $\delta^{13}C$ range for particulate terrestrial organic matter (-25 ‰ to –33 ‰; Salomons and Mook, 1981; Middelburg et al., 1997; Barth et al., 1998). Therefore, the shelf and slope sediments appear to contain an admixture of terrestrially and marine derived organic matter. For the basin, the

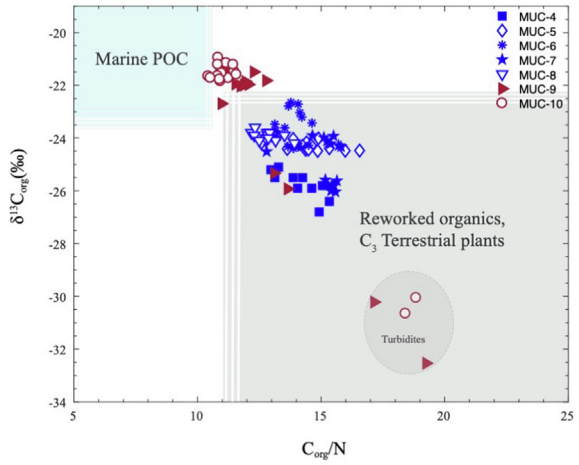

Fig. 8. Shelf-to-basin distribution of organic carbon stable isotope ($\delta^{13}C_{org}$) and C_{org}/N ratio to determine the organic matter source. Organic matter source boundaries adapted from Lamb et al. (2006). Carbon isotopes reported in delta notation relative to Pee Dee Belemnite (PDB). Nitrogen isotopes reported in delta notation relative to $N_{2(air)}$.

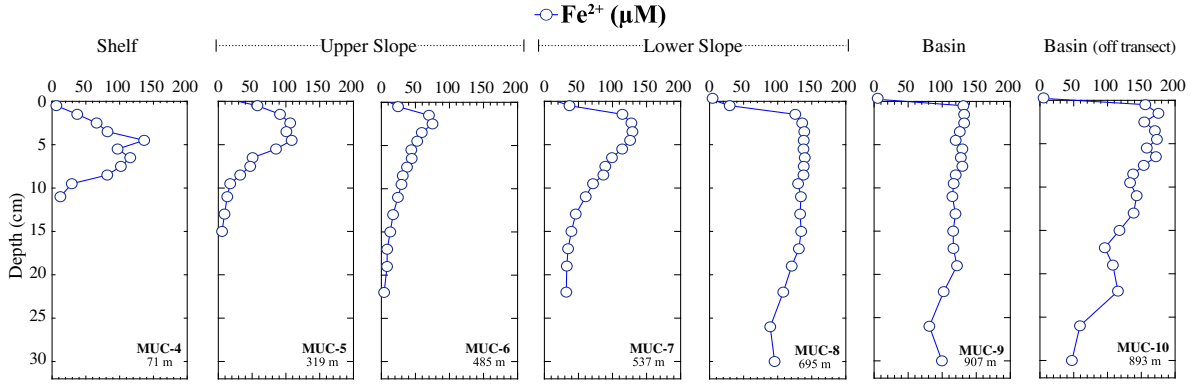

Fig. 7. Porewater Fe^{2+} concentration profiles.

Table 3
Iron values for all core-top samples and calculated diffusive fluxes of Fe^{2+} across the sediment–water interface.

Site	Water depth (m)	Sample ID	Fe/Al (0–1 cm)	Fe_{HR}/Fe_T (0–1 cm)	Fe^{2+} (μM) (0–1 cm)	BW Fe^{2+} (μM)	Fe efflux (μmol m^{-2} d^{-1})	Porosity (0–1 cm)
Shelf	71	MUC-4	0.45	0.14	6.31	BD	27.8	0.64
Slope	319	MUC-5	0.62	0.19	57.8	BD	180.0	0.76
Slope	485	MUC-6	0.62	0.38	24.5	BD	49.0	0.86
Slope	537	MUC-7	0.51	0.18	36.8	BD	112.3	0.77
Slope	695	MUC-8	0.64	0.40	29.5	0.3	66.0	0.84
Basin	907	MUC-9	0.83	0.54	131.1	0.9	200.2	0.92
Basin	893	MUC-10	1.10	0.64	155.9	0.3	206.1	0.91

C_{org}/N ratio is slightly higher than typical marine ratios of ≤ 10 (Thornton and McManus, 1994; Schubert and Calvert, 2001; Brodie et al., 2011; Leng and Lewis, 2017), yet the $\delta^{13}C$ values are well within those typical of marine organic matter (-16 ‰ to −23 ‰ $\delta^{13}C$; Lamb et al., 2006; Collins et al., 2011; Brodie et al., 2011; Leng and Lewis, 2017), suggesting that the organic matter from the basin sediments are mainly marine-sourced with some contribution of terrigenous input and progressively marine reworked organic matter.

Radiocarbon data from core-top sediments from the shelf, slope, and base of the slope (MUC-4, −6, and −8, respectively) were analyzed for comparison with the basin sediments (Table 4). The shelf and slope have lighter $\Delta^{14}C$ and higher $^{14}C_{age}$ values compared to the core-top sediments from the basin. The lowest part of the slope (MUC-8) has the oldest apparent $^{14}C_{age}$ (1885 ± 20 yrBP), and the basin (MUC-9) has the youngest $^{14}C_{age}$ (375 ± 20 yrBP). This suggests that continuous downslope mass transport tends to result in deposition at the lowest part of the slope, where MUC-8 was collected, while the turbidite layers from the deep basin are more characteristic of past sporadic events. The radiocarbon calibration for age correction (Table 4) reveals that the basin sediments (MUC-9, −10) have a strong decrease in $\Delta^{14}C$ and increase in $^{14}C_{age}$ between the surface sediments and sediments below 5 cm depth.

3.4. Reactive-transport model results

3.4.1. Model validation

The model-data fit is shown in Fig. 9 for MUC 9. In brief, the model closely reproduces the measured CH_2O (TOC) profile (Fig. 9a), excluding the turbidite layer (>25 cm). The sulfate-fitted profile matches strongly with the measured data (Fig. 9b). The estimated sulfide content and measured data show small differences within the first centimeters (Fig. 9c), nevertheless, the comparison shows that sulfide levels are overall low, and that the highest accumulation occurs near 2.5 cm depth. The estimated precipitated pyrite is close, although slightly lower, to the pyrite measured from the sediments (modeled mean = 0.07 ± 0.04 wt%; measured mean = 0.13 ± 0.07 wt% FeS_2; Fig. 9f). Considering that the model is only accounting for newly formed pyrite, both the modeled and measured profiles are consistent with little formation of pyrite with depth. The modeled Fe^{2+} concentration within the first centimeter appears to be an order of magnitude lower compared to the measured concentration; however, below 1 cm, the concentrations closely match those measured (Fig. 9d). Similarly, the estimated [FeOOH] is higher than the measured FeOOH (the sum of Fe_{asc} and Fe_{dith} fractions; Fig. 9e) within the top sediment, by about 5.5 wt% more FeOOH, but matched the measured values below 1 cm.

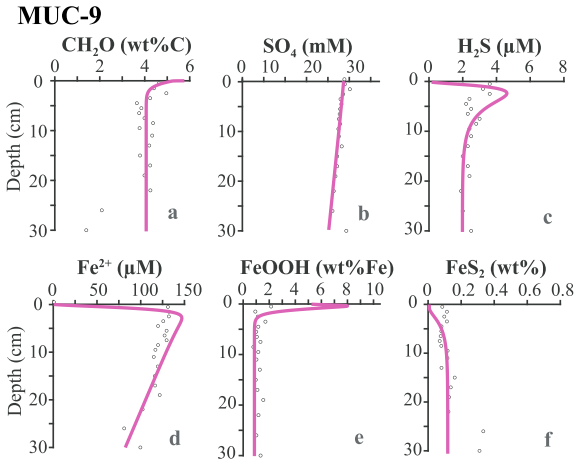

Fig. 9. Concentration depth profiles of sediment porewater solutes and solids. Open markers indicate measured data, while continuous solid lines represent model simulated depth profiles.

It is important to note that our model assumes that the sediment is in steady state. However, the processes and related products occurring within a very narrow interval at the sediment–water interface are influenced by strong seasonal controls compared to deeper sedimentary layers. In fact, another recent field study at the same field site in 2008 recorded FeOOH concentrations of up to 7 wt% (Burdige and Komada, 2020), which is similar to our modeled concentrations (Fig. 9e). It is also important to note that our model only considers two types of FeOOH minerals and a simplified reaction network. For example, we do not simulate the OM-Fe interactions that occur near the sediment–water interface (partly because those reactions are not yet fully understood). Ultimately, while it is important to be aware of the model-data discrepancies, the biogeochemical model is able to reproduce the

Table 4
Radiocarbon values and modeled values for bulk organic carbon from the sediments.

Core ID	Sediment mid-depth (cm)	Fraction Modern	±	^{14}C age (BP)	±	$\Delta^{14}C$ (‰)	±	Modelled calendar years (AD)	
								From	To
MUC-04	0.5	0.850	0.002	1305	20	−157.1	1.9	980	1128
MUC-06	0.5	0.867	0.002	1140	20	−139.6	1.8	1147	1286
MUC-08	0.5	0.791	0.002	1885	20	−215.8	1.8	388	545
MUC-09	0.5	0.954	0.002	375	20	−53.7	2.1	1819	>1950
	5.5	0.849	0.002	1315	20	−158.1	1.8	968	1117
	7.5	0.859	0.002	1225	20	−148.5	1.9	1053	1204
	11	0.838	0.002	1420	20	−169.1	1.7	850	1011
	13	0.828	0.002	1520	20	−179.2	1.7	744	899
	15	0.825	0.002	1545	20	−181.6	1.8	722	874
	19	0.801	0.002	1780	20	−205.6	1.7	494	651
	22	0.791	0.002	1880	20	−215.4	1.8	394	548
MUC-10	0.5	0.948	0.002	430	20	−59.8	2.1	1735	>1950
	5.5	0.840	0.002	1405	20	−167.2	2.0	872	1024
	6.5	0.850	0.002	1300	20	−156.6	1.9	985	1132
	11	0.831	0.002	1487	20	−176.0	1.8	767	921
	13	0.820	0.002	1600	20	−187.2	1.8	680	805
	15	0.676	0.002	3145	25	−329.7	1.7	−1154	−971
	19	0.683	0.002	3060	20	−322.4	1.6	−1031	−861
	26	0.767	0.002	2125	20	−238.8	1.7	99	250

main data trends and is a tool that can extract quantitative rates from our dataset.

3.4.2. Organic matter remineralization

The model estimates an input of POC to the sediment at 1.6 mmol C/m^{-2} d^{-1}, of which 44 % is remineralized and 56 % is buried (estimated POC flux of 0.70 mmol m^{-2} d^{-1}). The burial efficiency (BE = OM_{burial}/OM_{input}*100) of 56 % is in close agreement with previous field studies from this location (~50 %; Jahnke, 1990; Berelson et al., 1996). The fraction of POC that is not buried is oxidized within the first 5 cm. The DIC efflux, estimated from the surveyed 30 cm sediment depth (of 0.70 mmol m^{-2} d^{-1}), is however lower than previously measured fluxes collected using in-situ deployed benthic lander systems (~1.4 mmol m^{-2} d^{-1}; Jahnke, 1990; Berelson et al., 1996).

Despite O_2 concentration being low in the overlying water (4.4 μM), the estimated O_2 influx of 0.58 mmol m^{-2} d^{-1} produces an oxygen penetration depth of ca. 2 mm (oxygen penetration depth defined as the depth where [O_2] < 1 μM), supporting organic matter oxidation through aerobic respiration (and conceivably nitrate reduction) within the first millimeters of sediments. Note that the model does not account for denitrification or manganese reduction that could also oxidize organic matter, Fe^{2+}, and perhaps H_2S. In a nitrate transport study, (Prokopenko et al., (2011) reported that foraminifera in the adjacent San Pedro Basin sediment transport bottom water nitrate into the surface sediments as deep as ~ 5 cm, where it is denitrified to N_2. This denitrification may also be coupled to the oxidation of organic matter in the SMB sediments (see also Risgaard-Petersen et al., 2006; Piña-Ochoa et al., 2010) and may account for the higher DIC fluxes measured from benthic chambers (e.g., Jahnke, 1990; Berelson et al., 1996). However, since Fe^{2+} accumulates immediately below the sediment–water interface, the role of nitrate and Mn oxides as oxidants are likely minor in this system.

Iron reduction occurs mainly within the first 3 cm depth below the sediment–water interface (Fig. 10). We observe that the main source for DFe is sulfide-mediated FeOOH reduction (328.8 μmol Fe m^{-2} d^{-1}) and dissimilatory FeOOH reduction is a minor fraction (49.6 μmol Fe m^{-2} d^{-1}). Most of the sulfide that is produced from sulfate reduction (81.0 μmol S m^{-2} d^{-1}) is oxidized (46.9 μmol S m^{-2} d^{-1}) immediately below the surface from sulfide oxidation (5.8 μmol S m^{-2} d^{-1}) mostly by reductive dissolution of Fe oxides (41.1 μmol S m^{-2}·d^{-1}), effectively buffering the concentration of sulfide to lower levels and allowing build-up of Fe^{2+}. Due to the limited build-up of sulfide in the sediment, a significant portion of the DFe escapes to the overlying waters, with an estimated Fe flux of 200 μmol Fe m^{-2} d^{-1}.

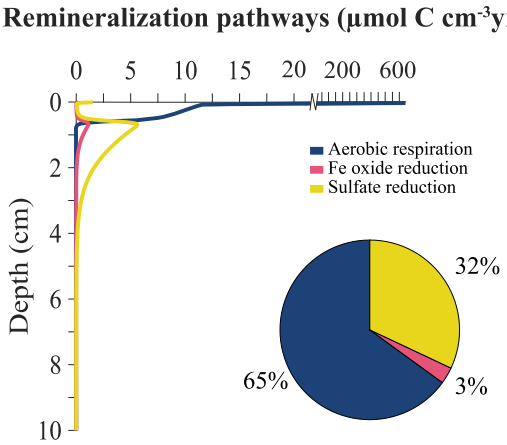

Fig. 10. Depth profiles of the rates of the different organic matter remineralization pathway rates. Inlayed, relative contribution of remineralization pathways.

3.4.3. Model experiments

To assess the stability of the SMB as an Fe-dominated system, we designed three model experiments to evaluate the impact of changing bottom-water O_2 (O_{2BW}), POC flux, and reactive OM efficiency on dissolved Fe (DFe) inventory and benthic Fe flux (Fig. 11). We also include a figure in the Supplementary Material (Figure S3) of the modeled geochemical profile for FeOOH, Fe^{2+}, H_2S, and FeS_2 under changing O_{2BW}, POC flux, and reactive OM efficiency.

In the model experiment with changing O_{2BW} (Fig. 11, top), the highest DFe content is identified at the baseline O_2 concentration of 4.4 μM. An increase in O_2 (>4.4 μM) causes the DFe inventory to decrease gradually, with 22 μM O_2 still containing significant DFe accumulation (1.6 μmol cm^{-2}). However, decreasing bottom water O_2 towards anoxia sharply decreases the DFe inventory and leads to a sulfide-dominated regime where most of the DFe diffuses and escapes to the water column and the rest reacts with sulfide to form iron sulfides.

The estimated influx of POC to the sediment is 1.6 mmol C/m^{-2} d^{-1}, of which only 44 % is remineralized within the first 5 cm, and the rest is buried. Consequently, the reactive POC flux and our baseline flux, is 0.70 mmol C/m^{-2} d^{-1}. For changes in POC flux (Fig. 11, middle), the highest levels of DFe are detected at a POC flux range of 0.35–0.70 mmol m^{-2} d^{-1}. An increase in POC flux from our baseline flux (0.70 mmol m^{-2} d^{-1}) leads to a sharp decrease in DFe, meaning that increasing reactive POC delivery (without increasing sedimentation rate) can lead to more effective organic matter oxidation near the sediment–water interface, thus shallowing the oxygen penetration depth and allowing for H_2S accumulation at a shallower sediment depth, therefore decreasing the accumulation of DFe, increasing Fe flux, and leading to more sulfide-dominated conditions.

The model experiment with changing fractions of reactive OM efficiency is illustrated in Fig. 11 (bottom) by the relationship between Fe and the fraction of slowly reactive OM. We observe that increasing the slowly reactive OM fraction, from the baseline fraction of 0.4, gradually decreases DFe accumulation without substantially decreasing the Fe flux. Increasing the slowly reactive OM fraction pushes most of the electron accepting processes closer to the sediment–water interface, consuming the highly reactive OM quickly and leading to a more reducing environment where sulfide dominates. Conversely, decreasing the slowly reactive OM fraction to lower levels creates an environment that is reductant-limited, and neither iron nor sulfide will dominate. The strongest DFe accumulation occurs when the delivery of reactive OM consists of up of 60–80 % rapidly reactive organic material. However, at 80 % rapid reactivity (i.e., 20 % slowly reactive OM) most of the carbon is oxidized at the sediment–water interface, leading to diminishing POC fluxes to the underlying sediments, which will lower DFe accumulation and reduce diffusive Fe fluxes to the overlying water.

4. Discussion

4.1. Potential factors for low sulfide detection

4.1.1. Sulfide oxidation

The sediments in the deep basin of SMB exhibit an extended ferruginous zone defined by low reduced sulfur (FeS_x, H_2S) and a strong enrichment of highly reactive Fe oxides and Fe^{2+} in the porewater despite being deposited under oxygen-deficient conditions with no bioturbation; having the potential to be a strongly reducing environment. An unexplored mechanism for the persis-

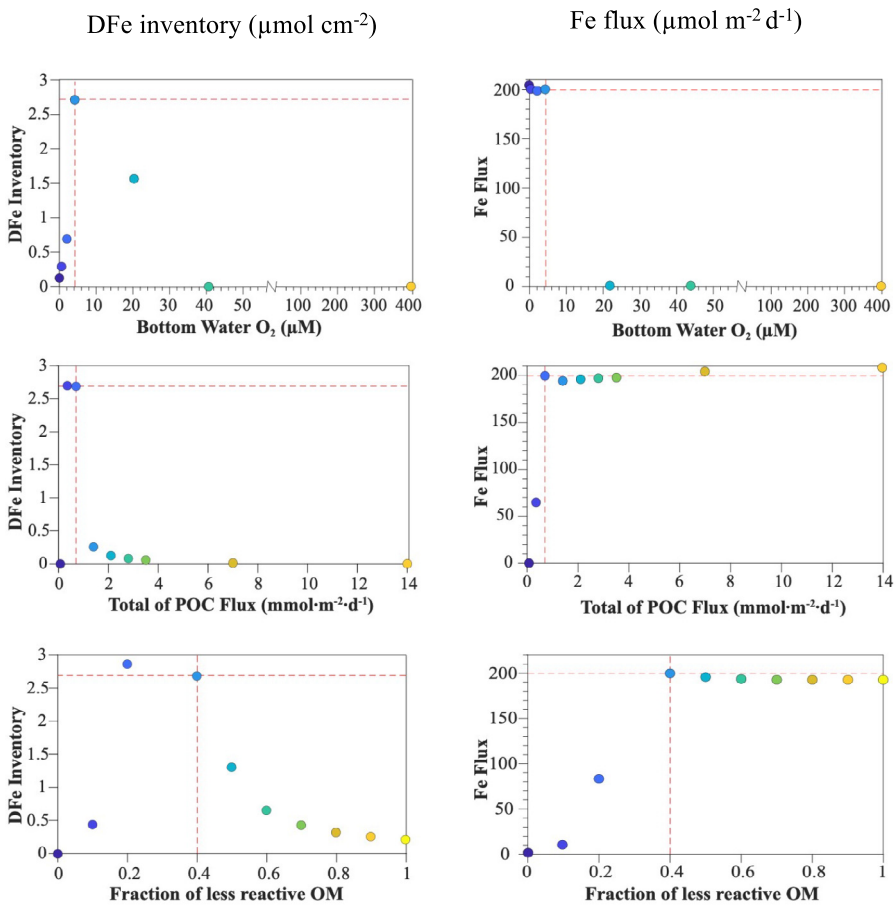

Fig. 11. Modeled sensitivity of DFe inventory and Fe flux under changing bottom water O_2 concentration (top), reactive POC flux (middle), and fraction of less reactive organic matter (bottom). The intersection between the dashed red lines corresponds to our data baseline.

tent lack of reduced sulfur and persistent high levels of sulfate could be the presence of microbially mediated sulfide oxidation.

Cable bacteria activity, for example, has been documented in sediments with similar chemical profiles—that is, surface sediments enriched in Fe oxide and low sulfide at depth (Seitaj et al., 2015; Reguera, 2018; Hermans et al., 2019). Cable bacteria transform the sediments by oxidizing sulfide and acidifying the porewater, causing iron-sulfides to dissolve and allowing the resulting Fe^{2+} to diffuse upwards to the oxic zone where it precipitated as iron oxides (Risgaard-Petersen et al., 2012; Seitaj et al., 2015; Reguera, 2018). This process usually draws down the pH in porewaters, which has been documented for sediments in SMB by Jahnke (1990) as a decrease from 7.8 to $\leq$ 7.2 within the first 5 cm of the sedimentary profile. The decrease in pH could also be attributed to other processes such as CO_2 release during organic matter oxidation. Furthermore, sulfide oxidation by cable bacteria can only extend to about 7 cm depth (van de Velde et al., 2016). Given this limitation, it is unlikely that cable bacteria could produce the extended (~30 cm deep) inhibition in sulfide accumulation in our basin sediments.

Other sulfide oxidizing microbes such as *Thioploca* spp. and *Beggiatoaceae* could also account for sulfide oxidation and concomitant Fe oxide formation. However, there was no visible indication of sulfur oxidizing microbes when we sampled the sediment cores. Further, another study (Prokopenko et al., 2011) was unable to detect sulfur oxidizing bacteria. The only visual identifications of *Thioploca* spp. in SMB were reported approximately 30 and 20 years ago (Craven and Jahnke, 1992; Pearson et al., 2001). Amplicon sequencing for microbial ecology is thus needed to determine whether microbially induced sulfide oxidation does occur in the SMB sediments. Notably, our model determined that sulfide-mediated FeOOH reduction is the main pathway for sulfide oxidation and Fe^{2+} production; however, microbial characterization would provide evidence as to whether any microbial activity is influencing sulfide oxidation or if this reaction is solely abiotic.

4.1.2. Organic carbon reactivity

Our measured and modeled data suggest that organic carbon reactivity is a limiting factor in sulfide accumulation. Data from the geochemical tracers (C_{org}/N, $\delta^{13}C_{org}$, and radiocarbon data) suggest that organic carbon deposited in the basin is mainly marine-sourced, yet with some contributions of terrestrial and recycled marine particulate matter (see Section 3.2). The $\Delta^{14}C$ data from the core-tops (-53.7 ± 2.1 ‰ for MUC-9) are not consistent with the $\Delta^{14}C$ of the overlying surface water DIC (71 ± 3 ‰; Pearson et al., 2000), suggesting that a portion of the organic matter is allochthonous with some degree of recalcitrance. Additionally, the $\Delta^{14}C$ values from the organic carbon below 5 cm significantly decrease, suggesting that most of the young and reactive organic carbon gets consumed above that depth (Table 4). This observation agrees with the measured chemical data and modeled results indicating that most of the terminal electron accepting processes take place within the top 5 cm, consuming most of the highly reactive organic carbon. The underlying sediments, consequently, contain an accumulation of a less reactive organic matter pool.

Consequently, the reactive POC flux (0.7 mmol C/m^{-2} d^{-1}) is mostly consumed before dissimilatory sulfate reduction can predominate, limiting the amount of sulfide produced. To contrast, if all the POC reaching the sediment (1.6 mmol C/m^{-2} d^{-1}) were reactive, then the POC flux would support higher sulfate reduction rates and a sulfide-dominated environment (see Section 3.3.4). Furthermore, our model prescribes two fractions for the reactive organic carbon pool, with 60 % being rapidly reactive. The suggestion is that a significant fraction of this carbon is quickly remineralized below the sediment–water interface mainly by aerobic respiration (see Fig. 10), further limiting sulfate reduction rates.

Importantly, the detection of Fe(III)-OM coprecipitates in the basin sediments and their high abundance (approx. one third of total Fe; see Section 3.1.2) suggests an important mechanism for preservation of organic carbon in the sediment and inhibiting its reactivity. These organometallic structures are particularly stable under anaerobic conditions and survive degradation for hundreds to thousands of years (Lalonde et al., 2012), serving as extremely efficient sinks for organic carbon. Within our sedimentary profile, these complexes are most abundant at shallow depths (0–1 cm depth) and are comprised mostly of the ferrihydrite-like Fe(III)-OM-1 complex, while the bottom sediments (28–30 cm depth) show a decrease of this phase, with the organic carbon- enriched Fe(III)-OM-2 complex becoming predominant. These observations align well with the amount of highly reactive FeOOH observed from sequential Fe extraction (Fe_{asc} and Fe_{dith}) and validate the retention of FeOOH and organic matter with depth. Ultimately, these results show that organic carbon reactivity below 5 cm depth is limited, which slows sulfate reduction rates and concomitant sulfide accumulation.

4.2. Iron delivery and enrichment in the sediments

The sediments in the deep basin of the SMB are enriched in reactive FeOOH relative to the shelf and slope. Several processes could contribute to the net accumulation of reactive Fe such as (1) lateral transport of dissolved and/or particulate Fe from the shelf and slope (Lyons and Severmann, 2006; Scholz et al., 2019) and (2) enhanced authigenic FeOOH formation by upward diffusion of Fe^{2+}. Our calculated diffusion fluxes estimate a benthic Fe flux rate of 200 μmol Fe m^{-2} d^{-1}, while FeOOH enters the sediment at an estimated flux rate of 210 μmol Fe m^{-2} d^{-1}. The slightly higher influx of FeOOH relative to the DFe efflux suggests that a fraction of the reactive FeOOH is allochthonous, possibly from lateral transport and preferential transport of fine-grained Fe-rich particles (e.g., Scholz et al., 2019). Moreover, the Fe/Al ratios, Fe_{HR}/Fe_T ratios, and benthic Fe fluxes from the shelf and slope show evidence for significant release of Fe to the water column (Table 3 and Fig. 12). Even with oxic bottom-water, shelf and slope-derived Fe (shuttle-derived) can be transferred to the basin and deposited at the seafloor (Scholz, 2018; Scholz et al., 2019). Accordingly, our data indicate that lateral transport (Fe shuttle) is a significant factor for the enrichment in highly reactive Fe in the basin. Similar to the observation from the semi-restricted Guaymas Basin (Scholz et al., 2019), bathymetric restriction and lack of water mass transport out of the basin further ensures an Fe trap towards sedimentary Fe enrichment.

The Santa Monica Basin can experience episodic bottom water O_2 variability that can allow FeOOH in-growth below the sediment–water interface during increased oxidation periods. For example, Elrod et al. (2004) measured Fe fluxes during times when

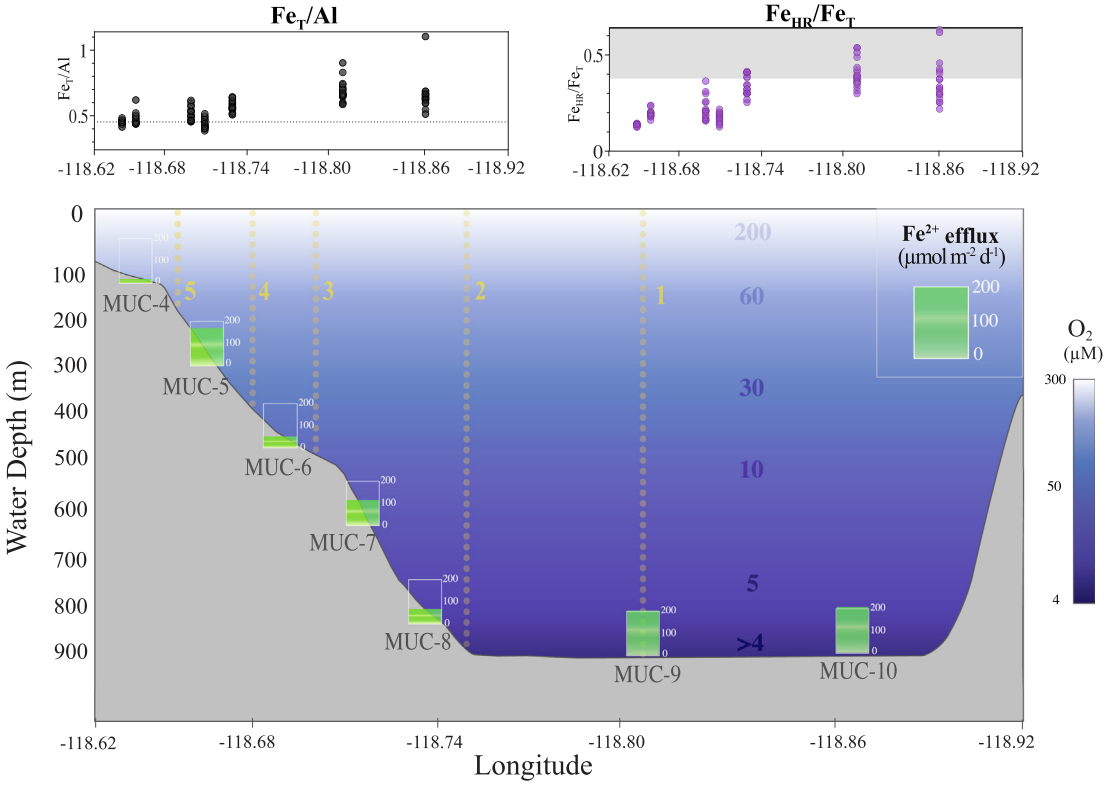

Fig. 12. Iron content for all sediment core stations. Top left: Fe_T/Al plot, the dashed line represents the upper continental crust value (Fe_T/Al = 0.44; Rudnick and Gao, 2014). Top right: Fe_{HR}/ Fe_T plot, the shaded portion represents Fe_{HR}/ Fe_T > 0.38, the suggested threshold (Raiswell et al., 2018) for modern sediments under anoxic/ferruginous conditions. Bottom: cross section of the Santa Monica Basin with dissolved O_2 concentrations in backdrop. The yellow dotted lines represent the CTD stations (see Table 1). The green bars represent the benthic Fe^{2+} efflux within the sediment–water interface, see Table 3 for more details.

the deep basin had higher bottom water O_2 concentration (9–10 μM) and observed a large offset between lower benthic chamber Fe flux (18 μmol m^{-2} d^{-1}) and higher potential DFe diffusion flux from porewater Fe^{2+} concentration gradient (289 μmol m^{-2} d^{-1}). During this time, a large fraction of the DFe diffusing upward must have been oxidized and precipitated below the sediment surface before it could enter the chamber. We can expect that once the bottom waters become more reduced, a fraction of the authigenic FeOOH will be reduced and diffuse towards the surface where it can be re-oxidized to form amorphous FeOOH, eventually settling back into the sediments.

The low levels of bottom water O_2 are crucial for the continuous Fe redox (re)cycling at the sediment–water interface, ultimately leading to a strong enrichment of FeOOH. Notably, the temporal increase in bottom-water O_2 that this basin occasionally experiences is still low enough (~10 μM; Elrod et al., 2004) to sustain accumulation of Fe^{2+} in the porewater below the sediment surface yet limiting the escape of Fe^{2+} via upward diffusion to the overlying water and instead enhancing precipitation of authigenic FeOOH (e.g., ferrihydrite) at the surface. These small pulses of oxygen ensure a strong accumulation of FeOOH within the surface sediments, followed by an enhanced diffusive Fe flux toward the sediment–water interface during lower bottom water O_2 concentrations. By contrast, if the bottom-water becomes more reducing (≤2.2 μM O_2; Fig. 11), the Fe (re)cycling within the sediment–water interface would be inhibited, decreasing reactive Fe enrichment. Similarly, increasing bottom-water O_2 towards oxic levels will also inhibit the Fe (re)cycling near the sediment–water interface, mainly by restricting Fe^{2+} accumulation (Fig. 11 and Figure S3). Therefore, the low variability in the bottom-water O_2 levels that ensures an oxygen-deficient setting, yet not oxygen-depleted, is a key factor for sustaining sediments with elevated FeOOH and Fe^{2+} enrichment. Ultimately, lateral transport of reactive Fe to the basin, bathymetric restriction, and consistent oxygen-deficient bottom waters (4 – 10 μM O_2) are key factors for supporting the elevated reactive Fe accumulation in the SMB sediments.

4.3. The Fe-S cycling

The FeOOH enrichment in the SMB sediment is sufficiently high to support sulfide-mediated FeOOH reduction and buffer sulfide accumulation to lower levels. This reaction ($H_2S + 8FeOOH_x + 14H^+ \rightarrow SO_4^{2-} + 8Fe^{2+} + 12H_2O$) can occur when highly reactive FeOOH (e.g., ferrihydrite) is particularly abundant relative to sulfide (Canfield, 1989; Canfield et al., 1992; Mortimer et al., 2011). Fig. 13 shows the reaction rate profiles for Fe^{2+} and sulfide formed from dissimilatory Fe(III) and sulfate reduction, respectively, and the net accumulation of Fe^{2+} and sulfide that was measured, emphasizing the significance of the sulfide-mediated Fe(III) reduction in enhancing Fe^{2+} and lowering sulfide concentration. With increasing depth, the FeOOH decreases to levels where sulfide-mediated iron reduction is no longer favorable, and pyrite precipitation occurs at moderate rates, as is also mirrored in the associated decreases in Fe^{2+} and SO_4^{2-} despite low sulfate reduction rate (Fig. 13).

Consequently, the extended ferruginous zone ensures that a significant proportion of the authigenic Fe minerals remain unsulfurized. As suggested in previous studies (i.e., Mississippi delta; Canfield, 1989; Amazon shelf; Aller et al., 1986), formation of authigenic Fe minerals such as siderite, which is not a common diagenetic mineral in marine sediments deposited at times in Earth history marked by appreciable levels of marine sulfate, is a consequence of extensive zones of Fe(III) reduction without substantial sulfide production. Consistent with this possibility, we detected siderite in the SMB sediments via the Fe_{ace} extraction and in Mössbauer spectroscopy. Siderite formation today is commonly found in low sulfate and sulfide environments such as freshwater swamps, low salinity estuarine regions, and marine sediments buried below the sulfidic zone (Berner and Raiswell, 1983; Berner, 1984). However, we detail another possibility for siderite formation, specifically a high sulfate environment with limited organic matter reactivity that inhibits FeS_x formation and preserves FeOOH minerals. A similar system has been characterized from salt marsh sediments, where rapid burial promotes Fe(III) reduction over sulfate reduction, leading to the formation of siderite concretions (Mortimer et al., 2011). However, for the SMB sediments, our Mössbauer spectra detected only low levels of siderite (~4% of total Fe). More work involving alkalinity and carbonate speciation is needed to better understand the extent of authigenic $FeCO_3$ precipitation in the SMB sediments.

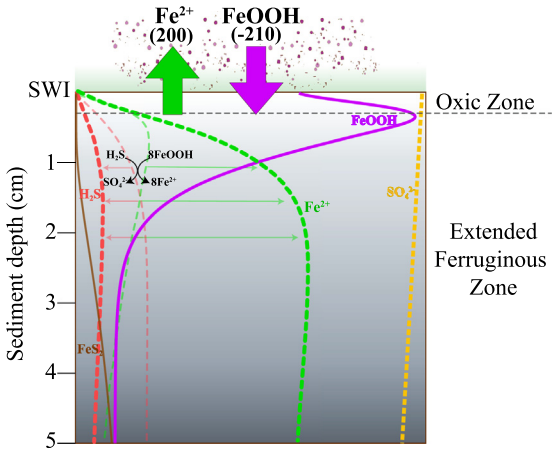

Fig. 13. Conceptual model explaining the chemical zones within the early diagenetic sediment depths of the deep basin. The large arrows crossing the sediment–water interface represent the dissolved Fe flux (green) and Fe oxide flux (magenta), the numbers in parenthesis are their respective fluxes in μmol $m^{-2}d^{-1}$. The efflux of dissolved Fe that makes it to the overlying water is represented by the green hue. The conversion of dissolved Fe to precipitated FeOOH and additional delivery of FeOOH from the water column is represented by the amorphous magenta particles sinking into the surface sediments. The thin and faded chemical profiles represent the production of porewater H_2S and Fe^{2+} from dissimilatory microbial reduction of Fe(III) and SO_4^{2-} (remineralization pathways). Sulfide-mediated Fe(III) reduction (simplified with black arrows) leads to further decrease of H_2S and enhanced accumulation of Fe^{2+}. At increasing depth, the highly reducible FeOOH eventually decreases to levels where sulfide-mediated Fe(III) reduction is no longer favorable, allowing for FeS_2 precipitation.

4.4. Implications for Fe-rich sediments

Other depositional systems along continental margins have been characterized by similar surface sediment enrichment of reactive FeOOH associated with low levels of sulfide in dissolved and solid-phase, such as the sediments off the Mississippi Delta (Canfield, 1989), the Argentine Basin (Riedinger et al., 2017), and Guaymas Basin (Scholz et al., 2019). However, in contrast to SMB, these environments have higher sedimentation rates and lower reactive organic matter delivery (~1% TOC, Riedinger et al., 2017) with frequent disturbance/reworking at the final site of deposition, resulting in lower remineralization rates and subsequent lower dissolved Fe (17.5 μM Fe^{2+} maximum in upper sediments, Riedinger et al., 2017). In comparison, relatively higher delivery of fresh marine OM in the SMB results in appreciable reactive organic carbon in the surface layers, which promotes relatively higher remineralization rates that lead to higher levels of Fe^{2+} and subsequent high DFe flux to the water column.

Furthermore, the elevated Fe shuttle and cycling within the SMB sediments contribute to the ample amount of reactive Fe oxides, Fe-carbonates (siderite), and Fe-rich silicate minerals, which were the mineral precursors and constituents of Precambrian iron formations (Koeksoy et al., 2016; Swanner et al., 2020). Consequently, our reported Fe_{HR}/Fe_T and Fe_{PY}/Fe_{HR} ratios correlate with those presumed to represent ferruginous water-column conditions from ancient sedimentary systems (Poulton and Canfield, 2011; Raiswell et al., 2018). The shared theme between our depositional setting and past Fe-rich settings is low O_2 availability. However, past Fe-rich systems are interpreted to have been controlled by water-column ferruginous conditions linked to low sulfate availability, whereas our findings provide an alternative mechanism where local controls linked to hypoxic bottom waters and limited organic matter reactivity result in Fe-rich sediments.

Notably, the SMB depositional system produces a redox signature similar to that described for ferruginous systems from Mid- and NeoProterozoic paleogeographic settings (e.g., Johnston et al., 2010; Planavsky et al., 2011; Reinhard et al., 2013; Guilbaud et al., 2015), when shallow epicontinental seas were abundant. The similarities are intriguing given the notable occurrence of (semi)restricted basins during the Mid- and NeoProterozoic (e.g., Johnston et al., 2010), inciting local differences in Fe supply, dissolved O_2 levels, and organic matter input; all important factors for redox conditions. Among intermediate oceanic settings such as the ones present today along continental margins and during the Mid- and NeoProterozoic, the variability in redox conditions reflect the significance of localized basin influences (Reinhard et al., 2013; Scholz et al., 2019; van de Velde et al., 2020) and a need for careful evaluation when interpreting paleoredox proxies such as the Fe proxy. As such, this study describes some of the intricate processes that can occur during early-diagenesis in restricted basins and their effect on the sedimentary record.

5. Conclusions

This study provides a thorough investigation of the C, Fe, and S biogeochemical processes in sediments of the Santa Monica Basin by exploring sediment geochemical data from the oxic slope to the hypoxic basin. The basin sediments appear to support an Fe-dominated redox cycle, characterized by persistent FeOOH enrichment and elevated dissolved Fe^{2+} accumulation despite being deposited under oxygen-deficient conditions with little or no bioturbation/bioirrigation but with active, yet limited, dissimilatory sulfate reduction. The prevalence of this Fe-dominated redox system is sustained by two key factors: (1) limited reactivity of the organic matter that is deposited and buried in the basin and (2) persistent hypoxic bottom waters with limited bottom water O_2 variability.

Most of the carbon remineralization processes occur within the first 5 cm. The youngest and most reactive organic matter is quickly remineralized within the surface sediments, limiting dissimilatory iron and sulfate reduction rates. The overall result is an extended ferruginous zone characterized by persistent Fe (oxyhydr)oxide and dissolved Fe^{2+} enrichment fueled by a strong Fe cycle concomitant with formation of ferrihydrite-like Fe(III)-OM coprecipitates, leading to further enhancement of organic matter preservation and FeOOH burial. Sulfate remains high, from the seawater value of 28 mM below the sediment water interface to 25 mM in the deepest sediments. Most of the sulfide formed via sulfate reduction is immediately consumed via oxidation coupled to the reduction of Fe(III). This step effectively buffers the concentration of sulfide to low levels while limiting pyrite formation and facilitating strong build-up of dissolved Fe. As a result, a significant efflux of Fe^{2+} is released to the overlying water column, and unsulfurized Fe minerals dominate in the sediments. Our observations and diagenetic modeling confirm that the trajectory (source-reworking-transport-sink relationships) of organic material can have a strong influence on the diagenetic processes in a given basin. The early diagenetic process described here may be an underappreciated pathway of Fe cycling in modern and ancient marine systems with important implications for the occurrence of Fe species in marine sediments and our corresponding ability to interpret the biogeochemical specifics of ancient environments.

Data availability

Research data is provided in the Supplementary Material.

Declaration of Competing Interest

The authors declare that they have no known competing financial interests or personal relationships that could have appeared to influence the work reported in this paper.

Acknowledgments

We thank the Southern California Marine Institute as well as the captain and crew of the R/V Yellowfin for logistical and technical support during the field sampling. We thank A. Joukhajian and K. Knight for their support during sediment core sub-sampling. Funding was provided by a NOAA Sea Grant (to W.B. and T.T, grant no. NA14OAR4170089), the Petroleum Research Fund of the American Chemical Society (T.W.L.), the NASA Interdisciplinary Consortia for Astrobiology Research (ICAR) Program (T.W.L.), a faculty research grant from the University of California Los Angeles (T.T.) and the NSERC Discovery grant (04843) to DDG. Mössbauer spectroscopy research was performed on a project award (EMSL-UP-50756) from the Environmental Molecular Sciences Laboratory, a DOE Office of Science User Facility sponsored by the Biological and Environmental Research program under Contract No. DE-AC05-76RL01830.

Appendix A. Supplementary material

Supplementary material to this article can be found online at https://doi.org/10.1016/j.gca.2022.11.026.

References

Aller, R.C., Mackin, J.E., Cox, R.T., 1986. Diagenesis of Fe and S in Amazon inner shelf muds: apparent dominance of Fe reduction and implications for the genesis of ironstones. Cont. Shelf Res. 6, 263–289.

Anderson, T.F., Raiswell, R., 2004. Sources and mechanisms for the enrichment of highly reactive iron in euxinic Black Sea sediments. Am. J. Sci. 304, 203–233.

Barth, J.A.C., Veizer, J., Mayer, B., 1998. Origin of particulate organic carbon in the upper St. Lawrence: isotopic constraints. Earth Planet. Sci. Lett. 162, 111–121.

Berelson, W.M., McManus, J., Coale, K.H., Johnson, K.S., Kilgore, T., Burdige, D., Pilskaln, C., 1996. Biogenic matter diagenesis on the sea floor: A comparison between two continental margin transects. J. Mar. Res. 54, 731–762.

Berelson, W., McManus, J., Coale, K., Johnson, K., Burdige, D., Kilgore, T., Colodner, D., Chavez, F., Kudela, R., Boucher, J., 2003. A time series of benthic flux measurements from Monterey Bay. CA. *Cont. Shelf Res.* 23, 457–481.

Berner, R.A., 1982. Burial of organic carbon and pyrite sulfur in the modern ocean; its geochemical and environmental significance. Am. J. Sci. 282, 451–473.

Berner, R.A., 1984. Sedimentary pyrite formation: An update. Geochim. Cosmochim. Acta 48, 605–615.

Berner, R.A., Raiswell, R., 1983. Burial of organic carbon and pyrite sulfur in sediments over phanerozoic time: a new theory. Geochim. Cosmochim. Acta 47, 855–862.

Boudreau, B.P., 1996. The diffusive tortuosity of fine-grained unlithified sediments. Geochim. Cosmochim. Acta 60, 3139–3142.

Brodie, C.R., Casford, J.S.L., Lloyd, J.M., Leng, M.J., Heaton Tim, H.E., Kendrick, C.P., Yongqiang, Z., 2011. Evidence for bias in C/N, δ13C and δ15N values of bulk organic matter, and on environmental interpretation, from a lake sedimentary sequence by pre-analysis acid treatment methods. Quat. Sci. Rev. 30, 3076–3087.

Burdige, D.J., Komada, T., 2020. Iron redox cycling, sediment resuspension and the role of sediments in low oxygen environments as sources of iron to the water column. Mar. Chem. 223, 103–793.
Canfield, D.E., 1989. Reactive iron in marine sediments. Geochim. Cosmochim. Acta 53, 619–632.
Canfield, D.E., Raiswell, R., Westrich, J.T., Reaves, C.M., Berner, R.A., 1986. The use of chromium reduction in the analysis of reduced inorganic sulfur in sediments and shales. Chem. Geol. 54, 149–155.
Canfield, D.E., Raiswell, R., Bottrell, S.H., 1992. The reactivity of sedimentary iron minerals toward sulfide. Am. J. Sci. 292, 659–683.
Chen, C., Kukkadapu, R., Sparks, D.L., 2015. Influence of Coprecipitated Organic Matter on $Fe^{2+}_{(aq)}$ -Catalyzed Transformation of Ferrihydrite: Implications for Carbon Dynamics. Environ. Sci. Technol. 49, 10927–10936.
Cline, J.D., 1969. Spectrophotometric Determination of Hydrogen Sulfide in Natural Waters. Limnol. Oceanogr. 14, 454–458.
Collins, L.E., Berelson, W., Hammond, D.E., Knapp, A., Schwartz, R., Capone, D., 2011. Particle fluxes in San Pedro Basin, California: A four-year record of sedimentation and physical forcing. *Deep Sea Res*. Part Oceanogr. Res. Pap. 58, 898–914.
Craven, D.B., Jahnke, R.A., 1992. Microbial utilization and turnover of organic carbon in Santa Monica Basin sediments. Prog. Oceanogr. 30, 313–333.
Elrod, V.A., Berelson, W.M., Coale, K.H., Johnson, K.S., 2004. The flux of iron from continental shelf sediments: A missing source for global budgets. Geophys. Res. Lett. 31.
Fossing, H., Jørgensen, B., 1989. Measurement of bacterial sulfate reduction in sediments: Evaluation of a single-step chromium reduction method. Biogeochemistry 8.
Froelich, P.N., Klinkhammer, G.P., Bender, M.L., Luedtke, N.A., Heath, G.R., Cullen, D., Dauphin, P., Hammond, D., Hartman, B., Maynard, V., 1979. Early oxidation of organic matter in pelagic sediments of the eastern equatorial Atlantic: suboxic diagenesis. Geochim. Cosmochim. Acta 43, 1075–1090.
Gorsline, D.S., 1992. The geological setting of Santa Monica and San Pedro Basins, California Continental Borderland. Prog. Oceanogr. 30, 1–36.
Gorsline, D.S., 1996. Depositional events in Santa Monica Basin, California Borderland, over the past five centuries. Sediment. Geol. 104, 73–88.
Gorsline, D.S., De Diego, T., Nava-Sanchez, E.H., 2000. Seismically triggered turbidites in small margin basins: Alfonso Basin, Western Gulf of California and Santa Monica Basin, California Borderland. Sediment. Geol. 135, 21–35.
Goya, G.F., Berquó, T.S., Fonseca, F.C., Morales, M.P., 2003. Static and dynamic magnetic properties of spherical magnetite nanoparticles. J. Appl. Phys. 94, 3520–3528.
Gregory, D.D., Lyons, T.W., Large, R.R., Jiang, G., Stepanov, A.S., Diamond, C.W., Figueroa, M.C., Olin, P., 2017. Whole rock and discrete pyrite geochemistry as complementary tracers of ancient ocean chemistry: An example from the Neoproterozoic Doushantuo Formation. China. *Geochim. Cosmochim. Acta* 216, 201–220.
Guilbaud, R., Poulton, S.W., Butterfield, N.J., Zhu, M., Shields-Zhou, G.A., 2015. A global transition to ferruginous conditions in the early Neoproterozoic oceans. Nat. Geosci. 8, 466–470.
Hardisty, D.S., Riedinger, N., Planavsky, N.J., Asael, D., Andren, T., Jørgensen, B.B., Lyons, T.W., 2016. A Holocene history of dynamic water column redox conditions in the Landsort Deep, Baltic Sea. Am. J. Sci. 316, 713–745.
Hardisty, D.S., Lyons, T.W., Riedinger, N., Isson, T.T., Owens, J.D., Aller, R.C., Rye, D.M., Planavsky, N.J., Reinhard, C.T., Gill, B.C., Masterson, A.L., Asael, D., Johnston, D.T., 2018. An evaluation of sedimentary molybdenum and iron as proxies for pore fluid paleoredox conditions. Am. J. Sci. 318, 527–556.
Henderson, G.M., 2002. New oceanic proxies for paleoclimate. Earth Planet. Sci. Lett. 203, 1–13.
Hepburn, L.E., Butler, I.B., Boyce, A., Schröder, C., 2020. The use of operationally-defined sequential Fe extraction methods for mineralogical applications: A cautionary tale from Mössbauer spectroscopy. Chem. Geol. 543, 119584.
Hermans, M., Lenstra, W.K., Hidalgo-Martinez, S., van Helmond, N.A.G.M., Witbaard, R., Meysman, F.J.R., Gonzalez, S., Slomp, C.P., 2019. Abundance and Biogeochemical Impact of Cable Bacteria in Baltic Sea Sediments. Environ. Sci. Technol. 53, 7494–7503.
Hua, Q., Barbetti, M., Rakowski, A.Z., 2013. Atmospheric Radiocarbon for the Period 1950–2010. Radiocarbon 55, 2059–2072.
Huh, C.-A., Zahnle, D.L., Small, L.F., Noshkin, V.E., 1987. Budgets and behaviors of uranium and thorium series isotopes in Santa Monica Basin sediments. Geochim. Cosmochim. Acta 51, 1743–1754.
Ingram, B.L., Southon, J.R., 1996. Reservoir Ages in Eastern Pacific Coastal and Estuarine Waters. Radiocarbon 38, 573–582.
Jahnke, R.A., 1990. Early diagenesis and recycling of biogenic debris at the seafloor, Santa Monica Basin. California. *J. Mar. Res.* 48, 413–436.
Johnston, D.T., Poulton, S.W., Dehler, C., Porter, S., Husson, J., Canfield, D.E., Knoll, A. H., 2010. An emerging picture of Neoproterozoic ocean chemistry: Insights from the Chuar Group, Grand Canyon, USA. Earth Planet. Sci. Lett. 290, 64–73.
Jørgensen, B.B., 1982. Mineralization of organic matter in the sea bed—the role of sulphate reduction. Nature 296, 643–645.
Jørgensen, B.B., Zawacki, L.X., Jannasch, H.W., 1990. Thermophilic bacterial sulfate reduction in deep-sea sediments at the Guaymas Basin hydrothermal vent site (Gulf of California). *Deep Sea Res*. Part Oceanogr. Res. Pap. 37, 695–710.
Kemnitz, N., Berelson, W., Hammond, D., Morine, L., Figueroa, M., Lyons, T.W., Scharf, S., Rollins, N., Petsios, E., Lemieux, S., Treude, T., 2020. Evidence of Changes in Sedimentation Rate and Sediment Fabric in a Low Oxygen Setting. Sediment, Santa Monica Basin, CA., Biogeochemistry.
Koeksoy, E., Halama, M., Konhauser, K.O., Kappler, A., 2016. Using modern ferruginous habitats to interpret Precambrian banded iron formation deposition. Int. J. Astrobiol. 15, 205–217.
Komada, T., Burdige, D.J., Crispo, S.M., Druffel, E.R.M., Griffin, S., Johnson, L., Le, D., 2013. Dissolved organic carbon dynamics in anaerobic sediments of the Santa Monica Basin. Geochim. Cosmochim. Acta 110, 253–273.
Kremling, K., 1999. Determination of the major constituents. In: Methods of Seawater Analysis. John Wiley & Sons, Ltd., pp. 229–251.
Lalonde, K., Mucci, A., Ouellet, A., Gélinas, Y., 2012. Preservation of organic matter in sediments promoted by iron. Nature 483, 198–200.
Lamb, A.L., Wilson, G.P., Leng, M.J., 2006. A review of coastal palaeoclimate and relative sea-level reconstructions using δ13C and C/N ratios in organic material. Earth-Sci. Rev. 75, 29–57.
Large, R.R., Halpin, J.A., Danyushevsky, L.V., Maslennikov, V.V., Bull, S.W., Long, J.A., Gregory, D.D., Lounejeva, E., Lyons, T.W., Sack, P.J., McGoldrick, P.J., Calver, C.R., 2014. Trace element content of sedimentary pyrite as a new proxy for deep-time ocean–atmosphere evolution. Earth Planet. Sci. Lett. 389, 209–220.
Leng, M.J., Lewis, J.P., 2017. C/N ratios and Carbon Isotope Composition of Organic Matter in Estuarine Environments. In: Weckström, K., Saunders, K.M., Gell, P.A., Skilbeck, C.G. (Eds.), Applications of Paleoenvironmental Techniques in Estuarine Studies. Developments in Paleoenvironmental Research. Springer, Netherlands, Dordrecht, pp. 213–237.
Li, C., Love, G.D., Lyons, T.W., Fike, D.A., Sessions, A.L., Chu, X., 2010. A Stratified Redox Model for the Ediacaran Ocean. Science 328, 80–83.
Lohan, M.C., Bruland, K.W., 2008. Elevated Fe(II) and dissolved Fe in hypoxic shelf waters off Oregon and Washington: an enhanced source of iron to coastal upwelling regimes. Environ. Sci. Technol. 42, 6462–6468.
Lyons, T.W., 1997. Sulfur isotopic trends and pathways of iron sulfide formation in upper Holocene sediments of the anoxic Black Sea. Geochim. Cosmochim. Acta 61, 3367–3382.
Lyons, T.W., Severmann, S., 2006. A critical look at iron paleoredox proxies: New insights from modern euxinic marine basins. Geochim. Cosmochim. Acta 70, 5698–5722.
Lyons, T.W., Anbar, A.D., Severmann, S., Scott, C., Gill, B.C., 2009. Tracking Euxinia in the Ancient Ocean: A Multiproxy Perspective and Proterozoic Case Study. Annu. Rev. Earth Planet. Sci. 37, 507–534.
Meysman, F.J.R., Boudreau, B.P., Middelburg, J.J., 2005. Modeling reactive transport in sediments subject to bioturbation and compaction. Geochim. Cosmochim. Acta 69, 3601–3617.
Middelburg, J.J., Nieuwenhuize, J., Lubberts, R.K., van de Plassche, O., 1997. Organic Carbon Isotope Systematics of Coastal Marshes. Estuar. Coast. Shelf Sci. 45, 681–687.
Mortimer, R.J.G., Galsworthy, A.M.J., Bottrell, S.H., Wilmot, L.E., Newton, R.J., 2011. Experimental evidence for rapid biotic and abiotic reduction of Fe (III) at low temperatures in salt marsh sediments: a possible mechanism for formation of modern sedimentary siderite concretions. Sedimentology 58, 1514–1529.
Murad, E., Cashion, J., 2004. Iron Oxides. In: Murad, E., Cashion, J. (Eds.), Mössbauer Spectroscopy of Environmental Materials and Their Industrial Utilization. Springer, US, Boston, MA, pp. 159–188.
Oueslati, W., van de Velde, S., Helali, M.A., Added, A., Aleya, L., Meysman, F.J.R., 2019. Carbon, iron and sulphur cycling in the sediments of a Mediterranean lagoon (Ghar El Melh, Tunisia). Estuar. Coast. Shelf Sci. 221, 156–169.
Pearson, A., Eglinton, T.I., McNichol, A.P., 2000. An organic tracer for surface ocean radiocarbon. Paleoceanography 15, 541–550.
Pearson, A., McNichol, A.P., Benitez-Nelson, B.C., Hayes, J.M., Eglinton, T.I., 2001. Origins of lipid biomarkers in Santa Monica Basin surface sediment: a case study using compound-specific Δ 14 C analysis. Geochim. Cosmochim. Acta 65, 3123–3137.
Peretyazhko, T.S., Zachara, J.M., Kukkadapu, R.K., Heald, S.M., Kutnyakov, I.V., Resch, C.T., Arey, B.W., Wang, C.M., Kovarik, L., Phillips, J.L., Moore, D.A., 2012. Pertechnetate ($TcO4^-$) reduction by reactive ferrous iron forms in naturally anoxic, redox transition zone sediments from the Hanford Site, USA. Geochim. Cosmochim. Acta 92, 48–66.
Piña-Ochoa, E., Hogslund, S., Geslin, E., Cedhagen, T., Revsbech, N.P., Nielsen, L.P., Schweizer, M., Jorissen, F., Rysgaard, S., Risgaard-Petersen, N., 2010. Widespread occurrence of nitrate storage and denitrification among Foraminifera and Gromiida. Proc. Natl. Acad. Sci. 107, 1148–1153.
Planavsky, N.J., McGoldrick, P., Scott, C.T., Li, C., Reinhard, C.T., Kelly, A.E., Chu, X., Bekker, A., Love, G.D., Lyons, T.W., 2011. Widespread iron-rich conditions in the mid-Proterozoic ocean. Nature 477, 448–451.
Poulton, S.W., Canfield, D.E., 2005. Development of a sequential extraction procedure for iron: implications for iron partitioning in continentally derived particulates. Chem. Geol. 214, 209–221.
Poulton, S.W., Canfield, D.E., 2011. Ferruginous Conditions: A Dominant Feature of the Ocean through Earth's History. Elements 7, 107–112.
Poulton, S.W., Krom, M.D., Raiswell, R., 2004. A revised scheme for the reactivity of iron (oxyhydr)oxide minerals towards dissolved sulfide. Geochim. Cosmochim. Acta 68, 3703–3715.
Prokopenko, M.G., Sigman, D.M., Berelson, W.M., Hammond, D.E., Barnett, B., Chong, L., Townsend-Small, A., 2011. Denitrification in anoxic sediments supported by biological nitrate transport. Geochim. Cosmochim. Acta 75, 7180–7199.
Raiswell, R., Berner, R.A., 1985. Pyrite formation in euxinic and semi-euxinic sediments. Am. J. Sci. 285, 710–724.
Raiswell, R., Canfield, D.E., 1998. Sources of iron for pyrite formation in marine sediments. Am. J. Sci. 298, 219–245.

Raiswell, R., Canfield, D.E., 2012. The Iron Biogeochemical Cycle Past and Present. Geochem. Perspect. 1, 1–220.
Raiswell, R., Canfield, D.E., Berner, R.A., 1994. A comparison of iron extraction methods for the determination of degree of pyritisation and the recognition of iron-limited pyrite formation. Chem. Geol. 111, 101–110.
Raiswell, R., Newton, R., Wignall, P.B., 2001. An Indicator of Water-Column Anoxia: Resolution of Biofacies Variations in the Kimmeridge Clay (Upper Jurassic, U.K.). J. Sediment. Res. 71, 286–294.
Raiswell, R., Vu, H.P., Brinza, L., Benning, L.G., 2010. The determination of labile Fe in ferrihydrite by ascorbic acid extraction: Methodology, dissolution kinetics and loss of solubility with age and de-watering. Chem. Geol. 278, 70–79.
Raiswell, R., Hardisty, D.S., Lyons, T.W., Canfield, D.E., Owens, J.D., Planavsky, N.J., Poulton, S.W., Reinhard, C.T., 2018. The iron paleoredox proxies: A guide to the pitfalls, problems and proper practice. Am. J. Sci. 318, 491–526.
Ramsey, C.B., 2009. Bayesian Analysis of Radiocarbon Dates. Radiocarbon 51, 337–360.
Rancourt, D.G., Ping, J.Y., 1991. Voigt-based methods for arbitrary-shape static hyperfine parameter distributions in Mössbauer spectroscopy. Nucl. Instrum. Methods Phys. Res. Sect. B Beam Interact. Mater. At. 58, 85–97.
Raven, M.R., Sessions, A.L., Fischer, W.W., Adkins, J.F., 2016. Sedimentary pyrite δ34S differs from porewater sulfide in Santa Barbara Basin: Proposed role of organic sulfur. Geochim. Cosmochim. Acta 186, 120–134.
Reguera, G., 2018. Biological electron transport goes the extra mile. Proc. Natl. Acad. Sci. 115, 5632–5634.
Reimer, P.J., Bard, E., Bayliss, A., Beck, J.W., Blackwell, P.G., Ramsey, C.B., Buck, C.E., Cheng, H., Edwards, R.L., Friedrich, M., Grootes, P.M., Guilderson, T.P., Haflidason, H., Hajdas, I., Hatté, C., Heaton, T.J., Hoffmann, D.L., Hogg, A.G., Hughen, K.A., Kaiser, K.F., Kromer, B., Manning, S.W., Niu, M., Reimer, R.W., Richards, D.A., Scott, E.M., Southon, J.R., Staff, R.A., Turney, C.S.M., van der Plicht, J., 2013. IntCal13 and Marine13 Radiocarbon Age Calibration Curves 0–50,000 Years cal BP. Radiocarbon 55, 1869–1887.
Reinhard, C.T., Planavsky, N.J., Robbins, L.J., Partin, C.A., Gill, B.C., Lalonde, S.V., Bekker, A., Konhauser, K.O., Lyons, T.W., 2013. Proterozoic ocean redox and biogeochemical stasis. Proc. Natl. Acad. Sci. 110, 5357–5362.
Rickard, D., Luther, G.W., 2007. Chemistry of Iron Sulfides. Chem. Rev. 107, 514–562.
Rickard, D., Morse, J.W., 2005. Acid volatile sulfide (AVS). Mar. Chem. 97, 141–197.
Riedinger, N., Brunner, B., Krastel, S., Arnold, G.L., Wehrmann, L.M., Formolo, M.J., Beck, A., Bates, S.M., Henkel, S., Kasten, S., Lyons, T.W., 2017. Sulfur Cycling in an Iron Oxide-Dominated, Dynamic Marine Depositional System: The Argentine Continental Margin. *Front*. Earth Sci. 5.
Risgaard-Petersen, N., Langezaal, A.M., Ingvardsen, S., Schmid, M.C., Jetten, M.S.M., Op den Camp, H.J.M., Derksen, J.W.M., Piña-Ochoa, E., Eriksson, S.P., Nielsen, L.P., Revsbech, N.P., Cedhagen, T., van der Zwaan, G.J., 2006. Evidence for complete denitrification in a benthic foraminifer. Nature 443, 93–96.
Risgaard-Petersen, N., Revil, A., Meister, P., Nielsen, L.P., 2012. Sulfur, iron-, and calcium cycling associated with natural electric currents running through marine sediment. Geochim. Cosmochim. Acta 92, 1–13.
Rudnick, R.L., Gao, S., 2014. 4.1 - Composition of the Continental Crust. In: Treatise on Geochemistry. Second Edition. Elsevier, Oxford, pp. 1–51.
Sack, P.J., Large, R.R., Gregory, D.D., 2018. Geochemistry of shale and sedimentary pyrite as a proxy for gold fertility in the Selwyn basin area, Yukon. Miner. Deposita 53, 997–1018.
Salomons, W., Mook, W.G., 1981. Field observations of the isotopic composition of particulate organic carbon in the southern North Sea and adjacent estuaries. Mar. Geol. 41, M11–M20.
Scholz, F., 2018. Identifying oxygen minimum zone-type biogeochemical cycling in Earth history using inorganic geochemical proxies. Earth-Sci. Rev. 184, 29–45.
Scholz, F., Schmidt, M., Hensen, C., Eroglu, S., Geilert, S., Gutjahr, M., Liebetrau, V., 2019. Shelf-to-basin iron shuttle in the Guaymas Basin, Gulf of California. Geochim. Cosmochim. Acta 261, 76–92.
Schubert, C.J., Calvert, S.E., 2001. Nitrogen and carbon isotopic composition of marine and terrestrial organic matter in Arctic Ocean sediments: implications for nutrient utilization and organic matter composition. Deep Sea Res. Part Oceanogr. Res. Pap. 48, 789–810.
Seitaj, D., Schauer, R., Sulu-Gambari, F., Hidalgo-Martinez, S., Malkin, S.Y., Burdorf, L. D.W., Slomp, C.P., Meysman, F.J.R., 2015. Cable bacteria generate a firewall against euxinia in seasonally hypoxic basins. Proc. Natl. Acad. Sci. 112, 13278–13283.
Severmann, S., McManus, J., Berelson, W.M., Hammond, D.E., 2010. The continental shelf benthic iron flux and its isotope composition. Geochim. Cosmochim. Acta 74, 3984–4004.
Soetaert, K., Herman, P.M.J., Middelburg, J.J., 1996. A model of early diagenetic processes from the shelf to abyssal depths. Geochim. Cosmochim. Acta 60, 1019–1040.
Soetaert, K., Meysman, F., 2012. Reactive transport in aquatic ecosystems: Rapid model prototyping in the open source software R. Environ. Model. Softw. 32, 49–60.
Stuiver, M., Polach, H.A., 1977. Discussion Reporting of 14C Data. Radiocarbon 19, 355–363.
Swanner, E.D., Lambrecht, N., Wittkop, C., Harding, C., Katsev, S., Torgeson, J., Poulton, S.W., 2020. The biogeochemistry of ferruginous lakes and past ferruginous oceans. Earth-Sci. Rev. 211, 103430.
Thornton, S.F., McManus, J., 1994. Application of Organic Carbon and Nitrogen Stable Isotope and C/N Ratios as Source Indicators of Organic Matter Provenance in Estuarine Systems: Evidence from the Tay Estuary, Scotland. Estuar. Coast. Shelf Sci. 38, 219–233.
van de Velde, S., Lesven, L., Burdorf, L.D.W., Hidalgo-Martinez, S., Geelhoed, J.S., Van Rijswijk, P., Gao, Y., Meysman, F.J.R., 2016. The impact of electrogenic sulfur oxidation on the biogeochemistry of coastal sediments: A field study. Geochim. Cosmochim. Acta 194, 211–232.
van de Velde, S., Meysman, F.J.R., 2016. The Influence of Bioturbation on Iron and Sulphur Cycling in Marine Sediments: A Model Analysis. Aquat. Geochem. 22, 469–504.
van de Velde, S.J., Reinhard, C.T., Ridgwell, A., Meysman, F.J.R., 2020. Bistability in the redox chemistry of sediments and oceans. Proc. Natl. Acad. Sci. 117, 33043–33050.
van de Velde, S., Van Lancker, V., Hidalgo-Martinez, S., Berelson, W.M., Meysman, F. J.R., 2018. Anthropogenic disturbance keeps the coastal seafloor biogeochemistry in a transient state. Sci. Rep. 8, 5582.
Zhao, Q., Callister, S.J., Thompson, A.M., Kukkadapu, R.K., Tfaily, M.M., Bramer, L.M., Qafoku, N.P., Bell, S.L., Hobbie, S.E., Seabloom, E.W., Borer, E.T., Hofmockel, K.S., 2020. Strong mineralogic control of soil organic matter composition in response to nutrient addition across diverse grassland sites. Sci. Total Environ. 736, 137839.
Zhao null, Huggins null, Feng null and Huffman null 1996. Surface-induced superparamagnetic relaxation in nanoscale ferrihydrite particles. Phys. Rev. B Condens. Matter 54, 3403–3407.